

Comparative analysis of critical regions for the renormalized quark-meson model with and without Polyakov loop potential

Akanksha Tripathi^{1,*} and Vivek Kumar Tiwari^{1,†}

¹*Department of Physics, University of Allahabad, Prayagraj, India-211002*

(Dated: December 16, 2025)

The critical regions enveloping the critical end point (CEP) in the μ -T plane of phase diagrams, have been mapped by drawing the contours of the normalized quark number susceptibility in the on-shell renormalized 2+1 flavor quark meson model (RQM) and Polyakov loop enhanced renormalized Polyakov quark meson (RPQM) model when $m_\sigma = 400$ and 500 MeV. The renormalized 't Hooft coupling c gets significantly stronger when the meson self energies due to quark loops are computed using the pole masses of mesons and parameters are fixed on shell in the Ref. [141] after consistent treatment of the quark one-loop vacuum fluctuation for the RQM model where the light and strange chiral symmetry breaking strengths also become weaker. The impact of the above novel features on the critical fluctuations have been computed. The improved PolyLog-glue form of the Polyakov loop potential of the Ref. [46], is employed to study the effect of the quark back reaction on critical fluctuations and results are compared with the scenario where quark back reaction is absent in the RPQM model with the Log form of the Polyakov loop potential. Using the large N_c standard chiral perturbation theory inputs, the phase diagrams are computed in the light chiral limit $m_\pi = 0$ and the proximity of the tricritical point (TCP) with the CEP is quantified in the μ -T plane. The RQM/RPQM model critical regions are compared with those reported in the Ref. [118] by different treatment of quark one-loop vacuum term where curvature masses of mesons are used to fix the parameters of the quark meson(QM)/Polyakov quark meson (PQM) model.

I. INTRODUCTION

Strong interaction theory known as the Quantum Chromodynamics (QCD), has entirely different properties in different energy regimes. The quarks and gluons, as the basic units of QCD, interact through weak coupling constant of color charge exchange for extremely high energies where perturbation theory works. The quark and gluons remain confined inside the hadrons in the low energy non-perturbative vacuum of QCD when the QCD coupling constant becomes large. Hadrons being the low energy degrees of freedom of QCD, get dissolved into their quark and gluon constituents for extremely high densities and temperatures, and such QCD phase transition [1–5] yields the color conducting plasma of quarks and gluons (QGP). The QCD phase transition studies are highly relevant for understanding the early universe evolution, the structure of compact stars, and the nature of the strong interaction. Since the theory is non-perturbative, the theoretical constructions of QCD phase transition rely mostly upon the two important properties of QCD called the phenomenon of spontaneous breaking of chiral symmetry and color charge confinement. The first principal Lattice QCD simulations performed at zero baryon densities [6–16] reveal important information and insights for the mapping of QCD phase structure in terms of chiral symmetry broken and restored phases as well as color charge confined and deconfined phases. But the LQCD simulations get severely compromised at non-zero

densities due to the fermion sign problem [17]. The QCD-like theoretical models [18–24], constructed in terms of effective degrees of freedom respecting different symmetries of QCD, constitute the required framework for the study of QCD phase diagram and associated critical phenomenon.

The Lagrangian of QCD has a global $SU_{L+R}(3) \times SU_{L-R}(3)$ symmetry when three flavor of quarks are massless. The formation of strange and non-strange chiral condensates, leads to the spontaneous breaking of the chiral $SU_A(3)$ symmetry yielding an octet of the massless pseudoscalar Goldstone bosons. Chiral symmetry is broken explicitly also due to small mass of the light u , d quarks and a relatively large mass of the s quark. Hence the experimentally observed three light pions, four relatively heavy kaons and a heavier η meson, are called the pseudo-Goldstone modes. The $U_A(1)$ anomaly caused by the instanton effects break the axial $U_A(1)$ symmetry explicitly at the quantum level and the η' meson becomes heavy with about 1 GeV mass [25], even if the three quarks are massless. The very useful effective theory framework of 2+1 flavor quark meson (QM) model [26] is obtained when the light u , d quarks and the s quark are coupled to the nine scalar and nine pseudoscalar mesons of the three flavor linear sigma model [27–29]. The extensively used Nambu-Jona-Lasinio (NJL) model [30–32] is an equivalent description where mesons are not taken as the fields in the Lagrangian but are generated through the multi-quark point interactions.

Further the chiral models are coupled to a constant background of $SU_c(N)$ gauge field [2, 33–38] to mimic the physics of QCD color confinement in a statistical sense. Adding the free energy density from gluons in the form of Polyakov-loop potential [39, 40] to the QM

* akankshatripathi330@gmail.com

† vivekkr@gmail.com

model effective potential, one gets the unified framework of Polyakov loop augmented quark meson (PQM) [41–45] model where physics of both the chiral symmetry breaking-restoration and confinement-deconfinement transition can be studied. Recent studies in Refs. [46–50] improved the Polyakov-loop potential from a pure gauge potential to a unquenched glue potential where the effects of the quark back reaction are also included. This improvement gives rise to the linkage of confinement-deconfinement and chiral phase transitions at small temperatures and large chemical potentials [48].

Lattice QCD has settled [51–53] that the temperature axis QCD transition at $\mu = 0$ for the physical point (physical quark masses for the $\{(m_\pi, m_K) = (138, 496) \text{ MeV}\}$) is a crossover and the effective theory [54] predicted a first-order phase transition at lower T and higher μ on the chemical potential axis. Hence the $\mu - T$ plane of phase diagram has to have a CEP [55–57] at which the chiral crossover transition line ends to become the first order transition line afterwards. The critical fluctuations of such a CEP belong to the $Z(2)$ universality class of three-dimensional Ising model [58–60]. In the light chiral limit $m_{ud} = 0$ of zero mass for the u and d quarks, the temperature driven chiral phase transition at the $\mu = 0$ is of second order whose the static critical behavior lies in the $O(4)$ universality class of the spin models in three dimensions [54]. Hence the presence of a CEP for the two quark flavor QCD with physical quark mass implies that the two flavor massless QCD has a tricritical point (TCP) at which the second order transition line of the $O(4)$ critical points ends to give a first order transition afterward in the $\mu - T$ plane of the phase diagram. The situation is analogous in the 2+1 flavor QCD where s quark has its physical mass while $m_{ud} = 0$ and one finds TCP when $\mu = 0$ in the QCD-like renormalized quark meson (RQM) model [61–64] for the light chiral limit when kaon mass has its physical point value $m_K = 496 \text{ MeV}$ while the pion mass $m_\pi = 0$.

The early signatures of CEP were proposed and discussed in Refs. [65–69]. The multi-step beam energy scan (BES) program was launched at the Relativistic Heavy Ion Collider (RHIC), Brookhaven National Laboratory (BNL) USA, in 2010 to investigate the QCD phase diagram and search the CEP [70, 71]. The first and second phase BES-I and BES-II got completed respectively in 2014 and 2021 [72]. The baryon density susceptibility and factorial cumulants of the proton multiplicity fluctuations which are expected to constitute the signatures of the CEP, are measured experimentally in BES-II [73, 74]. The theoretical aspects of CEP physics are comprehensively reviewed in Refs. [75, 76]. The identification signatures of the CEP, are the large fluctuations in the event-by-event distributions of conserved quantities, such as the net charge, baryon number, and strangeness [77–80]. The higher order moments of event-by-event distributions of conserved quantities can be measured experimentally and thermodynamic susceptibilities can be connected to them. Nonequilibrium dynamics of the non-

Gaussian fluctuations near the CEP are of particular importance to track the signal [81–87]. The new approach based on the principle of maximum entropy has been developed to deal with the problem of the freeze-out of non-Gaussian fluctuations, in and out of equilibrium [85, 87].

The different aspects of QCD phase transition has been extensively studied in chiral models [28, 29, 88–102], two and 2+1 flavor QM/PQM models [26, 41–45, 103–106]. Dropping the effect of quark one-loop vacuum fluctuations in the QM model studies under the standard mean field approximation (s-MFA), one finds that the chiral phase transition at zero baryon density becomes first order in the chiral limit which is inconsistent with the theoretical arguments [54, 107]. This inconsistency got removed in Ref. [108] after the inclusion of quark one-loop vacuum fluctuation in the two flavor QM model. The effect of fermionic vacuum corrections had been studied earlier [109–111] in the context of finite temperature and density Yukawa theory. Several studies [50, 108, 112–128] reported that the QCD thermodynamics and its phase structure gets strongly influenced when the quark one-loop vacuum term is included in the QM/PQM model. The model parameters in these studies were fixed using curvature masses of mesons which are found by taking the double derivatives of the effective potential at its minimum. Since the effective potential is the generator of the n-point functions of the theory at zero external momenta, the curvature masses account for the contribution of quark one-loop vacuum corrections in the meson self energies at the zero momentum. In the light of the above consideration, the parameter fixing looks inconsistent in these studies of the quark meson/Polyakov quark meson with the vacuum term (QMVT/PQMVT) model. Different studies have pointed out [129–135] that the pole masses of mesons are the physical and gauge invariant ones. The consistent treatment of quark one-loop vacuum fluctuations got developed recently in the Refs. [135–140] for the two flavor and the Refs. [63, 64, 141–144] for the three (2+1) flavor of the QM/PQM model. In the above on-shell renormalized QM (RQM) and Polyakov loop enhanced QM (RPQM) models, the parameters are renormalized on-shell by matching the counter terms in the on-shell scheme with the corresponding counter terms in the modified minimal subtraction $\overline{\text{MS}}$ scheme when the mass parameter and the running couplings are put into the relation of the physical pole masses of the pseudoscalar mesons π , K , η , η' and the scalar σ meson.

The 't Hooft coupling c gets significantly enhanced in the RQM model [141] because the condensate dependent part of the $U_A(1)$ anomaly term gets modified when the meson self energies due to quark loops are calculated using the pole meson masses. Furthermore, the explicit symmetry breaking strength $h_x(h_y)$ gets weaker by a small (relatively large) amount. Due to the above novel features, the CEP shifts upward in the phase diagram of the RQM model [141, 142] where in contrast to the QMVT model results [115–118], the smoothing ef-

fect of the quark one-loop vacuum fluctuations, on the strength of chiral phase transition, is moderate. The upward shift of the CEP in the RQM model gets significantly enhanced due to the Polyakov loop potential in the renormalized Polyakov loop augmented quark meson (RPQM) model [142]. Placed higher up than the CEP found in the curvature mass based parametrized PQMVT model work of the Schaefer et. al. [118], the CEP in the RPQM model [142], lies closer to the range of critical point location given by the most recent results of different theoretical techniques: Padé resummations of the Taylor expansion in μ_B ($= 3\mu_f$) whose coefficients are calculated on the lattice [145], also using conformal maps [146], the hybrid lattice plus gauge-gravity correspondence approach [147] and the functional renormalization group approach [148], all indicate the existence of the critical point in the same region of the QCD phase diagram : $T_c \sim (100 - 110)$ MeV and $\mu_B \sim (420 - 650) \Leftrightarrow \mu_{CEP} \sim (140 - 217)$ MeV [74]. In the light of the above, it is important to map the critical regions around the RQM and RPQM model CEP.

Extending the recent work of the Ref. [142], the present work has three important motives, first is to compute the RQM/RPQM model phase diagrams in the light chiral limit $m_\pi = 0$ and locate the tricritical point (TCP) when the $m_\sigma = 400$ and 500 MeV. The light chiral limit phase diagrams will be compared with the RQM/RPQM model phase diagrams computed in the Ref. [142] for the parameters at the physical point. The Log and PolyLog-glue form of the Polyakov loop potentials without and with quark back reactions in respective order will be used in the RPQM model. The large N_c standard chiral perturbation theory inputs as in the Ref. [61–63] will be used for determining the changed values of the pion and kaon decay constants f_π and f_K when the $m_\pi = 0$ while $m_K = 496$ MeV in the light chiral limit. Our second goal is to find the extent of critical regions by computing the contours of enhanced normalized quark number susceptibilities around the critical end point (CEP) in the RQM/RPQM model phase diagrams for the $m_\sigma = 400$ and 500 MeV. The changing size and shape of the critical regions will be compared when the m_σ changes from 400 to 500 MeV in different model settings. The effect of the properly treated quark one-loop vacuum corrections on the critical regions will be quantified by comparing the QM and RQM model. The critical regions in the RPQM and RQM model will be compared to see the combined effect of the Polyakov loop potential and the quark one-loop vacuum corrections. The above mentioned combined effect depends on whether the quark back reaction is absent in the Log form or present in the improved PolyLog-glue form of the Polyakov loop potential in the RPQM model. Quantifying the proximity of the TCP to the CEP for the $m_\sigma = 400$ and 500 MeV in the RQM/RPQM model phase diagrams, will tell us whether the TCP will influence the critical fluctuations around the CEP or not. In order to see how different methods of treating the quark one-loop vacuum

fluctuations in the QM/PQM model, affect the size and shape of the critical regions, our third goal is to compare the RQM/RPQM model results with the Schaefer et. al. QMVT/PQMVT model results for the $m_\sigma = 400$ MeV in the Ref. [118] where curvature masses of mesons are used for parameter fixing and Log Polyakov-loop potential is taken with the $T_0 = 270$ MeV for the Pure Yang-Mills $SU_c(3)$ gauge theory.

The paper is organized as follows. Section II gives a brief recapitulation of the QM/PQM/RQM/RPQM model. Section II A contains different Polyakov-loop potentials. Section II B gives the RPQM model grand potential. The light chiral limit formula and fixing of model parameters are discussed in section II C. Section III contains results and discussion. The phase diagrams, CEP and TCP are discussed in section III A, size and shape of the critical regions in different scenarios are compared in the section III B, RQM/RPQM model critical regions are compared with those of the QMVT/PQMVT model in the section III C. Section IV presents the summary.

II. MODEL RECAPITULATION

The Polyakov loop augmented quark meson (PQM) model [42–45] is obtained when three flavor of quarks are coupled to the $SU_V(3) \times SU_A(3)$ symmetric meson fields and the temporal component of gauge field represented by the Polyakov loop potential. The Polyakov loop field Φ is defined by the thermal expectation value of color trace of Wilson loop in temporal direction as :

$$\Phi(\vec{x}) = \frac{1}{N_c} \langle \text{Tr}_c L(\vec{x}) \rangle, \quad \bar{\Phi}(\vec{x}) = \frac{1}{N_c} \langle \text{Tr}_c L^\dagger(\vec{x}) \rangle \quad (1)$$

here $L(\vec{x})$ is a $SU_c(3)$ color gauge group matrix in its fundamental representation.

$$L(\vec{x}) = \mathcal{P} \exp \left[i \int_0^\beta d\tau A_0(\vec{x}, \tau) \right] \quad (2)$$

Where \mathcal{P} is path ordering, A_0 is the temporal component of vector field and $\beta = T^{-1}$ [33]. As in the Ref. [39, 40], the homogeneous Polyakov loop fields $\Phi(\vec{x}) = \Phi = \text{constant}$ and $\bar{\Phi}(\vec{x}) = \bar{\Phi} = \text{constant}$.

The Lagrangian of Polyakov quark-meson (PQM) model contains the Lagrangian of quark meson model and the Polyakov loop potential $\mathcal{U}(\Phi, \bar{\Phi}, T)$ as :

$$\mathcal{L}_{PQM} = \mathcal{L}_{QM} - \mathcal{U}(\Phi, \bar{\Phi}, T). \quad (3)$$

The Lagrangian of QM model [26, 28, 45] is the following:

$$\mathcal{L}_{QM} = \bar{\psi} [i\gamma^\mu D_\mu - g T_a (\sigma_a + i\gamma_5 \pi_a)] \psi + \mathcal{L}(\mathcal{M}) . \quad (4)$$

Quarks couple with the uniform temporal background gauge field as the following $D_\mu = \partial_\mu - iA_\mu$ and $A_\mu = \delta_{\mu 0} A_0$ (Polyakov gauge), where $A_\mu = g_s A_\mu^a \lambda^a / 2$ with vector potential A_μ^a for color gauge fields. g_s is the $SU_c(3)$

gauge coupling and λ_a ($a = 1 \cdots 8$) are Gell-Mann matrices in the color space. The above coupling is absent for the pure QM model where $D_\mu \equiv \partial_\mu$. The Lagrangian for the $SU_V(3) \times SU_A(3)$ symmetric meson fields is the following.

$$\begin{aligned} \mathcal{L}(\mathcal{M}) = & \text{Tr}(\partial_\mu \mathcal{M}^\dagger \partial^\mu \mathcal{M} - m^2(\mathcal{M}^\dagger \mathcal{M})) \\ & - \lambda_1 [\text{Tr}(\mathcal{M}^\dagger \mathcal{M})]^2 - \lambda_2 \text{Tr}(\mathcal{M}^\dagger \mathcal{M})^2 \\ & + c[\det \mathcal{M} + \det \mathcal{M}^\dagger] + \text{Tr}[H(\mathcal{M} + \mathcal{M}^\dagger)] . \end{aligned} \quad (5)$$

The flavor blind Yukawa coupling g couples the flavor triplet quark fields ψ (color N_c -plet Dirac spinor) to the nine scalar and pseudo-scalar meson ξ fields $\sigma_a(\pi_a)$ of 3×3 complex matrix $\mathcal{M} = T_a \xi_a = T_a(\sigma_a + i\pi_a)$. $T_a = \frac{\lambda_a}{2}$ where λ_a ($a = 0, 1 \cdots 8$) are Gell-Mann matrices with $\lambda_0 = \sqrt{\frac{2}{3}} \mathbb{I}_{3 \times 3}$. The ξ field develops the non-zero vacuum expectation value $\bar{\xi}$ in the 0 and 8 directions. The $SU_L(3) \times SU_R(3)$ chiral symmetry is broken spontaneously by the condensates $\bar{\sigma}_0$ and $\bar{\sigma}_8$ and it is broken explicitly also by the external fields $H = T_a h_a$ with $h_0, h_8 \neq 0$. The change from the singlet octet (0, 8) to the non-strange strange basis (x, y) gives $x(h_x) = \sqrt{\frac{2}{3}} \bar{\sigma}_0(h_0) + \frac{1}{\sqrt{3}} \bar{\sigma}_8(h_8)$ and $y(h_y) = \frac{1}{\sqrt{3}} \bar{\sigma}_0(h_0) - \sqrt{\frac{2}{3}} \bar{\sigma}_8(h_8)$. Considering the thermal and quantum fluctuations of the quarks/anti-quarks and treating the mesons at mean field level, the QM model grand potential [26, 45], is obtained after adding the vacuum effective potential $U(x, y)$ with the quark/anti-quark contribution $\Omega_{q\bar{q}}$ at finite temperature T and quark chemical potential μ_f ($f = u, d, s$).

$$\Omega_{\text{MF}}(T, \mu) = U(x, y) + \Omega_{q\bar{q}}(T, \mu; x, y) . \quad (6)$$

$$\Omega_{q\bar{q}}(T, \mu; x, y) = \Omega_{q\bar{q}}^{\text{vac}} + \Omega_{q\bar{q}}^{T, \mu}(x, y) . \quad (7)$$

$$\begin{aligned} U(x, y) = & \frac{m^2}{2} (x^2 + y^2) - h_x x - h_y y - \frac{c}{2\sqrt{2}} x^2 y \\ & + \frac{\lambda_1}{2} x^2 y^2 + \frac{1}{8} (2\lambda_1 + \lambda_2) x^4 + \frac{1}{8} (2\lambda_1 + 2\lambda_2) y^4 . \end{aligned} \quad (8)$$

$$\Omega_{q\bar{q}}^{\text{vac}} = -2N_c \sum_f \int \frac{d^3 p}{(2\pi)^3} E_q \theta(\Lambda_c^2 - \vec{p}^2) . \quad (9)$$

$$\Omega_{q\bar{q}}^{T, \mu}(x, y) = -2N_c \sum_{f=u, d, s} \int \frac{d^3 p}{(2\pi)^3} T \left[\ln g_f^+ + \ln g_f^- \right] . \quad (10)$$

$$\Omega_{\text{QM}}(T, \mu, x, y) = U(x, y) + \Omega_{q\bar{q}}^{T, \mu}(x, y) . \quad (11)$$

The $g_f^\pm = \left[1 + e^{-E_f^\pm/T} \right]$ where $E_f^\pm = E_f \mp \mu_f$ and $E_f = \sqrt{p^2 + m_f^2}$ is the quark/anti-quark energy. The light (strange) quark mass $m_{u/d} = \frac{gx}{2}$ ($m_s = \frac{gy}{\sqrt{2}}$) and $\mu_u = \mu_d = \mu_s = \mu$. In the standard mean field approximation (s-MFA) where Dirac sea contribution is neglected, the quark one-loop vacuum term with ultraviolet

cut-off Λ_c in Eq. (9) is dropped in the quark meson (QM) model grand effective potential in Eq. (11). Several studies have used the minimal subtraction scheme to regularize the quark one-loop vacuum divergences after including the vacuum fluctuations in the extended mean field approximation (e-MFA) [108, 114–118, 121, 127] but the vacuum effective potential $\Omega_{\text{vac}}(x, y) = U(x, y) + \Omega_{q\bar{q}}^{\text{vac}}$ in their treatment, turns inconsistent as they fix the model parameters using curvature masses of mesons which are obtained by taking the double derivatives of the effective potential with respect to the different fields at its minimum. The above mentioned inconsistency becomes apparent when one notes that the calculation of the curvature masses, involves the evaluation of the meson self-energies at zero momentum because the effective potential is the generator of the n-point functions of the theory at vanishing external momenta [131, 135–142]. The Refs. [129, 130] has emphasized that the pole definition of the meson mass is the physical and gauge invariant one.

The consistent e-MFA RQM model effective potential will be used in the present work which is derived in our very recent works [141, 142] after relating the counter-terms in the $\overline{\text{MS}}$ scheme to those in the on-shell (OS) scheme [135–140]. The relations between the renormalized parameters of both the schemes are determined when the physical quantities (the on-shell pole masses of the $m_\pi, m_K, m_\eta, m_{\eta'}$ and m_σ , the pion and kaon decay constants f_π and f_K) are put into the relation of the $\overline{\text{MS}}$ running couplings and mass parameter. These relations are used as input when the effective potential is calculated using the modified minimal subtraction procedure. After the cancellation of the $1/\epsilon$ divergences, the vacuum effective potential $\Omega_{\text{vac}} = U(x_{\overline{\text{MS}}}, y_{\overline{\text{MS}}}) + \Omega_{\overline{\text{MS}}}^{q, \text{vac}} + \delta U(x_{\overline{\text{MS}}}, y_{\overline{\text{MS}}})$ in the $\overline{\text{MS}}$ scheme has been rewritten in Ref. [141] in terms of the scale Λ independent constituent quark mass parameters $\Delta_x = \frac{g_{\overline{\text{MS}}} x_{\overline{\text{MS}}}}{2}$ and $\Delta_y = \frac{g_{\overline{\text{MS}}} y_{\overline{\text{MS}}}}{\sqrt{2}}$ as the following.

$$\begin{aligned} \Omega_{\text{vac}}(\Delta_x, \Delta_y) = & \frac{m_0^2}{g_0^2} (2\Delta_x^2 + \Delta_y^2) - 2 \frac{h_{x0}}{g_0} \Delta_x - \sqrt{2} \frac{h_{y0}}{g_0} \Delta_y \\ & - 2 \frac{c_0}{g_0^3} \Delta_x^2 \Delta_y + 4 \frac{\lambda_{10}}{g_0^4} \Delta_x^2 \Delta_y^2 + 2 \frac{(2\lambda_{10} + \lambda_{20})}{g_0^4} \Delta_x^4 \\ & + \frac{(\lambda_{10} + \lambda_{20})}{g_0^4} \Delta_y^4 + \frac{2N_c \Delta_x^4}{(4\pi)^2} \left[\frac{3}{2} + \ln \left(\frac{\Lambda^2}{m_u^2} \right) + \ln \left(\frac{m_u^2}{\Delta_x^2} \right) \right] \\ & + \frac{N_c \Delta_y^4}{(4\pi)^2} \left[\frac{3}{2} + \ln \left(\frac{\Lambda^2}{m_u^2} \right) + \ln \left(\frac{m_u^2}{\Delta_y^2} \right) \right] . \end{aligned} \quad (12)$$

The scale Λ_0 gets fixed by requiring that the minimum of the RQM model effective potential does not shift from that of the QM model [141, 142] as :

$$\ln \left(\frac{\Lambda_0^2}{m_u^2} \right) + \mathcal{C}(m_\pi^2) + m_\pi^2 \mathcal{C}'(m_\pi^2) = 0 . \quad (13)$$

The terms $\mathcal{C}(m_\pi^2)$ and $\mathcal{C}'(m_\pi^2)$ and the derivations for the renormalized parameters $m_0^2 = (m^2 + m_{\text{FIN}}^2)$, $h_{x0} = (h_x + h_{x\text{FIN}})$, $h_{y0} = (h_y + h_{y\text{FIN}})$, $\lambda_{10} = (\lambda_1 + \lambda_{1\text{FIN}})$, $\lambda_{20} =$

$(\lambda_2 + \lambda_{2\text{FIN}})$ and $c_0 = (c + c_{\text{FINTOT}})$ are given in detail in Refs. [141, 142]. The m_{FIN}^2 , $h_{x\text{FIN}}$, $h_{y\text{FIN}}$, $\lambda_{1\text{FIN}}$, $\lambda_{2\text{FIN}}$ and c_{FINTOT} are the finite on-shell corrections in the parameters at the scale Λ_0 . The experimental values of the pseudo-scalar meson masses m_π , m_K , m_η , $m_{\eta'}$ ($m_\eta^2 + m_{\eta'}^2$), the scalar σ mass m_σ and the f_π , f_K as input determine the tree level QM model quartic couplings λ_1 , λ_2 , mass parameter m^2 , h_x , h_y and the coefficient c of the t'Hooft determinant term for the $U_A(1)$ axial anomaly [26, 28]. The parameter determination is explained in Refs. [141, 142] also.

The dressing of the meson propagator in the on-shell scheme gives rise to the renormalization of f_π , f_K and g , but they do not change as the $g_{\overline{\text{MS}}} = g_{\text{ren}} = g_0 = g$, $x_{\overline{\text{MS}}} = x$, $y_{\overline{\text{MS}}} = y$ at Λ_0 . Further $x_{\overline{\text{MS}}} = f_{\pi,\text{ren}} = f_\pi$ and $y_{\overline{\text{MS}}} = \frac{2f_{K,\text{ren}} - f_{\pi,\text{ren}}}{\sqrt{2}} = \frac{2f_K - f_\pi}{\sqrt{2}}$ at the minimum. Using $\Delta_x = \frac{g_x}{2}$ and $\Delta_y = \frac{g_y}{\sqrt{2}}$, the vacuum effective potential in the Eq. (12) can be written in terms of the x and y as :

$$\begin{aligned} \Omega_{\text{vac}}^{\text{RQM}}(x, y) = & \frac{(m^2 + m_{\text{FIN}}^2)}{2} (x^2 + y^2) - (h_x + h_{x\text{FIN}}) x \\ & - (h_y + h_{y\text{FIN}}) y - \frac{(c + c_{\text{FINTOT}})}{2\sqrt{2}} x^2 y + \frac{(\lambda_1 + \lambda_{1\text{FIN}})}{2} x^2 y^2 \\ & + \frac{\{2(\lambda_1 + \lambda_{1\text{FIN}}) + (\lambda_2 + \lambda_{2\text{FIN}})\} x^4}{8} + (\lambda_1 + \lambda_{1\text{FIN}} + \lambda_2 \\ & + \lambda_{2\text{FIN}}) \frac{y^4}{4} + \frac{N_c g^4 (x^4 + 2y^4)}{8(4\pi)^2} \left[\frac{3}{2} - \mathcal{C}(m_\pi^2) - m_\pi^2 \mathcal{C}'(m_\pi^2) \right] \\ & - \frac{N_c g^4}{8(4\pi)^2} \left[x^4 \ln \left(\frac{x^2}{f_\pi^2} \right) + 2y^4 \ln \left(\frac{2y^2}{f_\pi^2} \right) \right]. \end{aligned} \quad (14)$$

$$\Omega_{\text{RQM}}(T, \mu, x, y) = \Omega_{\text{vac}}^{\text{RQM}}(x, y) + \Omega_{q\bar{q}}^{T, \mu}(x, y). \quad (15)$$

The T and μ dependence of the x and y is obtained after searching the minima of grand effective potential in the Eq. (15) as $\frac{\partial \Omega_{\text{RQM}}}{\partial x} = \frac{\partial \Omega_{\text{RQM}}}{\partial y} = 0$. The expressions of curvature masses of the scalar and pseudo-scalar mesons for the RQM model are derived in Refs. [63, 141]. The equations of motion $\frac{\partial \Omega_{\text{vac}}^{\text{RQM}}}{\partial x} = 0 = \frac{\partial \Omega_{\text{vac}}^{\text{RQM}}}{\partial y}$ obtained from the Eq. (14), give the following expressions for the renormalized chiral symmetry breaking strengths h_{x0} and h_{y0} .

$$h_{x0} = m_{\pi, c}^2 f_\pi. \quad (16)$$

$$h_{y0} = \left(\sqrt{2} f_K m_{K, c}^2 - \frac{f_\pi}{\sqrt{2}} m_{\pi, c}^2 \right). \quad (17)$$

The expressions of the pion and kaon curvature masses

$m_{\pi, c}$ and $m_{K, c}$ are the following.

$$m_{\pi, c}^2 = m_\pi^2 \left\{ 1 - \frac{N_c g^2}{4\pi^2} m_\pi^2 \mathcal{C}'(m_\pi^2, m_u) \right\}. \quad (18)$$

$$\begin{aligned} m_{K, c}^2 = m_K^2 \left[1 - \frac{N_c g^2}{4\pi^2} \left\{ \mathcal{C}(m_\pi^2, m_u) + m_\pi^2 \mathcal{C}'(m_\pi^2, m_u) \right. \right. \\ \left. \left. - \left(1 - \frac{(m_s - m_u)^2}{m_K^2} \right) \mathcal{C}(m_K^2, m_u, m_s) + \right. \right. \\ \left. \left. \left(1 - \frac{f_\pi}{f_K} \right) \left(\frac{m_u^2 - m_s^2 + 2m_s^2 \ln(\frac{m_s}{m_u})}{m_K^2} \right) \right] \right]. \end{aligned} \quad (19)$$

The π and K curvature masses $m_{\pi, c} = 135.95$ MeV and $m_{K, c} = 467.99$ MeV are, respectively, smaller by 2.05 MeV and 28.01 MeV from their corresponding pole masses $m_\pi = 138$ MeV and $m_K = 496$ MeV [141, 142].

A. Different forms of Polyakov-loop potential

The confinement-deconfinement phase transition has been studied in the literature using different forms of the Polyakov-loop effective potential $\mathcal{U}(\Phi, \bar{\Phi}, T)$. Its simplest form is constructed by finding a potential which respects all the given symmetries and accounts for the spontaneously broken $Z(3)$ symmetry for the system in the deconfined phase [2, 34, 35]. The following polynomial form constitutes the minimal content of the Polyakov-loop potential.

$$\frac{\mathcal{U}_{\text{Poly}}}{T^4} = -\frac{b_2(T)}{2} \Phi \bar{\Phi} - \frac{b_3}{6} (\Phi^3 + \bar{\Phi}^3) + \frac{b_4}{4} (\Phi \bar{\Phi})^2, \quad (20)$$

the coefficients of the Eq. (20) are given by

$$b_2(T) = a_0 + a_1 \left(\frac{T_0}{T} \right) + a_2 \left(\frac{T_0}{T} \right)^2 + a_3 \left(\frac{T_0}{T} \right)^3, \quad (21)$$

where $a_0 = 6.75$, $a_1 = -1.95$, $a_2 = 2.625$, $a_3 = -7.44$, $b_3 = 0.75$ and $b_4 = 7.5$.

The above form is improved by adding the contribution from the integration of the $SU(3)$ group volume in the generating functional for the Euclidean action. The Haar measure is used to perform this integration which takes the form of a Jacobian determinant. Its logarithm is added as an effective potential to the action in the generating functional. The potential gets bounded from below for the large Φ and $\bar{\Phi}$ by the positive coefficient of the logarithm term. The logarithmic form of the Polyakov-loop potential [37, 40] has the following expression.

$$\begin{aligned} \frac{\mathcal{U}_{\text{Log}}}{T^4} = & b(T) \ln[1 - 6\Phi\bar{\Phi} + 4(\Phi^3 + \bar{\Phi}^3) - 3(\Phi\bar{\Phi})^2] \\ & - \frac{1}{2} a(T) \Phi \bar{\Phi}. \end{aligned} \quad (22)$$

The parameters of the polynomial and log form of the Polyakov-loop potential were determined [39, 40] by fitting the lattice data for pressure, entropy density as well

as energy density and the evolution of Polyakov-loop $\langle \Phi \rangle$ on the lattice in pure gauge theory. The coefficients of the Eq. (22) are the following [40],

$$a(T) = a_0 + a_1 \left(\frac{T_0}{T} \right) + a_2 \left(\frac{T_0}{T} \right)^2, \quad (23)$$

$$b(T) = b_3 \left(\frac{T_0}{T} \right)^3, \quad (24)$$

where $a_0 = 3.51$, $a_1 = -2.47$, $a_2 = 15.2$, $b_3 = -1.75$. It is pointed out that the log potential has qualitative consistency with the leading order result of the strong-coupling expansion [14]. Furthermore, since the potential diverges for $\Phi, \bar{\Phi} \rightarrow 1$, the Polyakov-loop always remains smaller than 1 and approaches this value asymptotically as $T \rightarrow \infty$.

The new Polyakov-loop effective potential was constructed in the Ref. [47] after incorporating the Polyakov-loop fluctuations as well. Its parameters are adjusted such that the longitudinal as well as the transverse susceptibilities are also reproduced in addition to the other existing lattice data. The following new expression of the PolyLog Polyakov-loop potential gets constructed in this work after the logarithmic term is added to the polynomial form of the Polyakov-loop potential.

$$\begin{aligned} \frac{\mathcal{U}_{\text{PolyLog}}}{T^4} = & b(T) \ln[1 - 6\Phi\bar{\Phi} + 4(\Phi^3 + \bar{\Phi}^3) - 3(\Phi\bar{\Phi})^2] \\ & + a_2(T)\Phi\bar{\Phi} + a_3(T)(\Phi^3 + \bar{\Phi}^3) + a_4(T)(\Phi\bar{\Phi})^2. \end{aligned} \quad (25)$$

In the PolyLog parametrization, the coefficients in the Eq. (25) are defined as :

$$a_i(T) = \frac{a_0^{(i)} + a_1^{(i)} \left(\frac{T_0}{T} \right) + a_2^{(i)} \left(\frac{T_0}{T} \right)^2}{1 + a_3^{(i)} \left(\frac{T_0}{T} \right) + a_4^{(i)} \left(\frac{T_0}{T} \right)^2} \quad (26)$$

$$b(T) = b_0 \left(\frac{T_0}{T} \right)^{b_1} \left[1 - e^{b_2 \left(\frac{T_0}{T} \right)^{b_3}} \right]. \quad (27)$$

The summary of the parameters is given in the Table I.

TABLE I. Parameters of the PolyLog Polyakov-loop potential have been taken from the Ref. [47].

PolyLog	$a_0^{(2)}$	$a_1^{(2)}$	$a_2^{(2)}$	$a_3^{(2)}$	$a_4^{(2)}$
	22.07	-75.7	45.03385	2.77173	3.56403
$a_0^{(3)}$	$a_1^{(3)}$	$a_2^{(3)}$	$a_3^{(3)}$	$a_4^{(3)}$	
-25.39805	57.019	-44.7298	3.08718	6.72812	
$a_0^{(4)}$	$a_1^{(4)}$	$a_2^{(4)}$	$a_3^{(4)}$	$a_4^{(4)}$	
27.0885	-56.0859	71.2225	2.9715	6.61433	
b_0	b_1	b_2	b_3		
-0.32665	5.8559	-82.9823	3.0		

The deconfinement phase transition is first order with $T_c^{\text{YM}} = T_0 = 270$ MeV for the pure gauge Yang-Mills theory. The first order transition becomes a crossover in

presence of the dynamical quarks. The parameter T_0 depends on the number of quark flavors and chemical potential in the full dynamical QCD [41, 46, 48, 49, 124] because it is linked to the mass-scale Λ_{QCD} that gets modified by the effect of the fermionic matter fields. The $T_0 \rightarrow T_0(N_f, \mu)$ has the following form of the number of flavor and chemical potential dependence.

$$T_0(N_f, \mu) = \hat{T} e^{-1/(\alpha_0 b(N_f, \mu))}, \quad (28)$$

with

$$b(N_f, \mu) = \frac{1}{6\pi} (11N_c - 2N_f) - b_\mu \frac{\mu^2}{(\hat{\gamma} \hat{T})^2}. \quad (29)$$

here the \hat{T} parameter is fixed at the scale τ , $\hat{T} = T_\tau = 1.77$ GeV and $\alpha_0 = \alpha(\Lambda)$ at a UV scale Λ . The $T_0(N_f = 0) = 270$ MeV gives $\alpha_0 = 0.304$ and $b_\mu \simeq \frac{16}{\pi} N_f$. The parameter $\hat{\gamma}$ governs the curvature of $T_0(\mu)$ with the systematic error estimation range $0.7 \lesssim \hat{\gamma} \lesssim 1$ [41, 49]. Massive flavors lead to suppression factors of the order $T_0^2/(T_0^2 + m^2)$ in the β -function. For 2+1 flavors and a current strange quark mass $m_s \sim 150$ MeV, one obtains $T_0(2+1) = 187$ MeV [41, 49].

The Polyakov-loop potential gets replaced by the QCD glue potential after the back reaction of the quarks is included in the full QCD with dynamical quarks. The Ref. [46] applied the FRG equations to the QCD and compared the pure gauge potential \mathcal{U}_{YM} to the “glue” potential $\mathcal{U}_{\text{glue}}$ where quark polarization was included in the gluon propagator and they found significant differences between the two potentials. However, it was observed that the two potentials are of the same shape and they can be mapped into each other by relating the temperatures of the two systems, T_{YM} and T_{glue} . Denoting the previous equations of the Polyakov-loop potential by \mathcal{U}_{YM} , the improved Polyakov-loop potential $\mathcal{U}_{\text{glue}}$ is constructed as [46] :

$$\frac{\mathcal{U}_{\text{glue}}}{T_{\text{glue}}^4}(\Phi, \bar{\Phi}, T_{\text{glue}}) = \frac{\mathcal{U}_{\text{YM}}}{T_{\text{YM}}^4}(\Phi, \bar{\Phi}, T_{\text{YM}}) \quad (30)$$

here the temperature T_{glue} is related to T_{YM} as

$$\frac{T_{\text{YM}} - T_c^{\text{YM}}}{T_c^{\text{YM}}} = 0.57 \frac{T_{\text{glue}} - T_c^{\text{glue}}}{T_c^{\text{glue}}} \quad (31)$$

The T_c^{glue} is the transition temperature for the unquenched case. The coefficient 0.57 comes from the comparison of the two effective potentials. T_c^{glue} lies within a range $T_c^{\text{glue}} \in [180, 270]$. In practice, one uses the replacement $T \rightarrow T_c^{\text{YM}}(1 + 0.57(\frac{T}{T_c^{\text{glue}}} - 1))$ in the right-hand side of the Polyakov-loop potentials where T_0 means T_c^{YM} and $(T \sim T_{\text{YM}})$ on the left side of the arrow while $(T \sim T_{\text{glue}})$ on the right side [142]. We have taken T_c^{glue} and T_0 both fixed at 187 MeV in our calculations for the 2+1 quark flavor as in the Ref. [41, 46].

B. RPQM Model

The Polyakov-loop potential becomes active only at non-zero temperatures, hence it does not affect the vacuum parameters of the chiral part of the effective potential. Only the finite temperature part $\Omega_{q\bar{q}}^{T,\mu}$ given by the Eq. (10) in the quark-antiquark contribution to the total effective potential, gets modified by the Polyakov loop potential.

$$\Omega_{q\bar{q}}^{T,\mu}(x, y, \Phi, \bar{\Phi}) = -2N_c \sum_q \int \frac{d^3 p}{(2\pi)^3} T \left[\ln g_f^+ + \ln g_f^- \right] \quad (32)$$

The $\Omega_{q\bar{q}}^{T,\mu}(x, y, \Phi, \bar{\Phi}) = \Omega_{q\bar{q}}(T, \mu; x, y, \Phi, \bar{\Phi})$ and new g_f^\pm being different from their earlier values in the Eq. (10), are the following :

$$g_f^+ = \left[1 + 3\Phi e^{-E_q^+/T} + 3\bar{\Phi} e^{-2E_q^+/T} + e^{-3E_q^+/T} \right], \quad (33)$$

$$g_f^- = \left[1 + 3\bar{\Phi} e^{-E_q^-/T} + 3\Phi e^{-2E_q^-/T} + e^{-3E_q^-/T} \right]. \quad (34)$$

$E_f^\pm = E_f \mp \mu_f$ and $E_f = \sqrt{p^2 + m_f^2}$ with $f = u, d, s$ represent the quark/antiquark energy. Here $m_u = m_d = \frac{g_x}{2}$ is the mass of the light quarks u, d and strange quark mass is $m_s = \frac{g_y}{\sqrt{2}}$. In this work we have considered $\mu_u = \mu_d = \mu_s = \mu$.

The vacuum effective potential $\Omega_{vac}(x, y) = U(x, y) + \Omega_{q\bar{q}}^{vac}$ after the on-shell renormalization in the RQM model becomes $\Omega_{vac}^{RQM}(x, y)$. The grand thermodynamic potential of the renormalized Polyakov loop enhanced quark meson (RPQM) model [142] is obtained when the PQM model Lagrangian of the Eq. (3) is used and the RQM model vacuum effective potential $\Omega_{vac}^{RQM}(x, y)$ in the Eq. (14) is added to the thermal contributions of quarks-antiquarks in the presence of the Polyakov loop potential.

$$\Omega_{RPQM}(T, \mu; x, y, \Phi, \bar{\Phi}) = \Omega_{vac}^{RQM}(x, y) + \Omega_{q\bar{q}}(T, \mu; x, y, \Phi, \bar{\Phi}) \quad (35)$$

When quark one-loop vacuum contribution is dropped in the s-MFA, one gets the PQM model grand thermodynamic potential after adding the meson contribution in Eq. (8) to the thermal contributions of quarks-antiquarks in the presence of the Polyakov loop potential as the following.

$$\Omega_{PQM}(T, \mu; x, y, \Phi, \bar{\Phi}) = U(x, y) + \Omega_{q\bar{q}}(T, \mu; x, y, \Phi, \bar{\Phi}) \quad (36)$$

The temperature T and chemical potential μ dependence of the non-strange condensate x , strange condensate y , Φ and $\bar{\Phi}$ are obtained in the RPQM and PQM model by optimizing the global minimum of the grand potential respectively in the Eq. (35) and Eq. (36) .

$$\begin{aligned} \frac{\partial \Omega_{RPQM/PQM}}{\partial x} &= \frac{\partial \Omega_{RPQM/PQM}}{\partial y} = \frac{\partial \Omega_{RPQM/PQM}}{\partial \Phi} \\ &= \frac{\partial \Omega_{RPQM/PQM}}{\partial \bar{\Phi}} = 0 \end{aligned} \quad (37)$$

The 2+1 flavor RPQM and PQM model phase diagram with Log form and PolyLog-glue form of the Polyakov loop potential, different thermodynamic quantities and critical end point have been calculated and presented in the ref.[142]. We will be using the above described 2+1 flavor RQM and RPQM model and extend our work to calculate the quark number susceptibility for evaluating the critical region around CEP in different model scenarios.

C. Light Chiral Limit

We have used the standard large N_c , $U(3)$ chiral perturbation theory (ChPT) inputs as in the Ref. [61–63] to find the pion and kaon decay constants f_π and f_K and the parameters of the QM/RQM model for the light chiral limit. Taking the values $(f_\pi, f_K) = (92.4, 113.0216)$ MeV at the physical point for $(m_\pi, m_K) = (138, 496)$ MeV and using the following set of equations,

$$f_\pi = f \left(1 + 4 \frac{L_5}{f^2} m_\pi^2 \right). \quad (38)$$

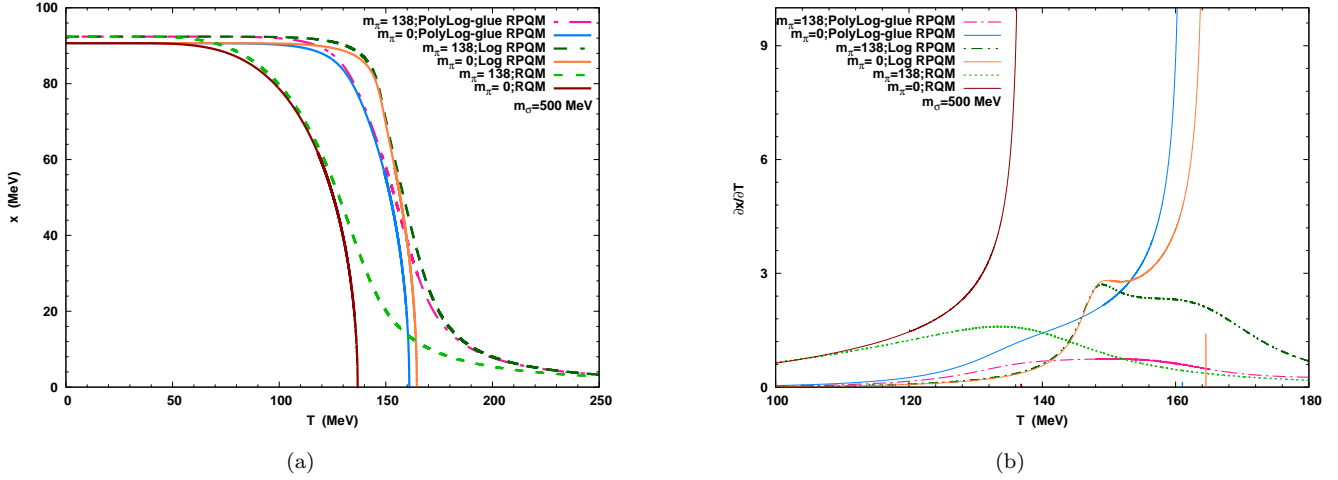
$$f_K = f \left(1 + 4 \frac{L_5}{f^2} m_K^2 \right). \quad (39)$$

one gets the $f = 90.67$ MeV and the chiral constant $L_5 = 2.06 \times 10^{-3}$ [61–63]. Chiral constants do not change when (m_π, m_K) are reduced to study the chiral limit while one move away from the physical point. The $f_\pi = f = 90.67$ MeV while $f_K = 113.0216$ MeV in the light chiral limit when $m_\pi = 0$ and $m_K = 496$ MeV.

For the physical point, RQM (QM) model parameters $\lambda_{20}(\lambda_2)$, $c_0(c)$, $h_{x0}(h_x)$, $h_{y0}(h_y)$, $m_0^2(m^2)$ and $\lambda_{10}(\lambda_1)$, are determined as in Refs. [63, 141, 142] taking the experimental values of the π, K, η and η' masses as $(m_\pi, m_K, m_\eta, m_{\eta'}) = (138, 496, 547.5, 957.78)$ MeV and choosing the scalar σ meson mass as $m_\sigma = 500$ MeV whereas the $f_\pi = 92.4$ MeV and $f_K = 113.0216$ MeV. Given the experimental masses $(m_\eta, m_{\eta'}) = (547.5, 957.78)$ MeV, one needs only the $M_\eta = \sqrt{(m_\eta^2 + m_{\eta'}^2)} = 1103.22$ MeV to find the parameters. One gets $m_\eta = 538.98$ MeV and $m_{\eta'} = 962.60$ MeV in the QM model after using its parameters determined at the physical point with $M_\eta = 1103.22$ MeV. Note that for the above M_η , when the pole masses $m_\eta = 527.58$ MeV and $m_{\eta'} = 968.89$ MeV are used as input in the RQM model for computing the η, η' self energy corrections and the renormalized parameters, the same pole

TABLE II. Different Model Parameters at the physical point and in the light chiral limit study.

Model	m_σ	m_π (MeV)	λ_2	$c(\text{MeV}^2)$	λ_1	$m^2(\text{MeV}^2)$	$h_x(\text{MeV}^3)$	$h_y(\text{MeV}^3)$
QM	400	138	46.43	4801.82	-5.89	$(494.549)^2$	$(120.73)^3$	$(336.43)^3$
	500	138	46.43	4801.82	-2.69	$(434.305)^2$	$(120.73)^3$	$(336.43)^3$
	500	0	44.62	4966.63	-0.96	$(411.663)^2$	0	$(340.05)^3$
RQM			λ_{20}	$c_0(\text{MeV}^2)$	λ_{10}	$m_0^2(\text{MeV}^2)$	$h_{x0}(\text{MeV}^3)$	$h_{y0}(\text{MeV}^3)$
	400	138	34.88	7269.20	1.45	$(442.447)^2$	$(119.53)^3$	$(323.32)^3$
	400	0	34.28	7485.73	2.03	$(437.090)^2$	0	$(329.83)^3$
	500	138	34.88	7269.20	3.676	$(396.075)^2$	$(119.53)^3$	$(323.32)^3$
	500	0	34.28	7485.73	4.622	$(382.143)^2$	0	$(329.83)^3$

FIG. 1. Temperature variations of the non-strange condensate x in [a] and it's derivative $\partial x/\partial T$ in [b] for the RQM, Log RPQM and PolyLog-glue RPQM model for the physical point $m_\pi = 138$ MeV and the light chiral limit $m_\pi = 0$ with $m_K = 496$ MeV.

masses for the η and η' are reproduced in the output after adding the corresponding self energy corrections to their respective masses calculated from the new set of renormalized parameters [141, 142]. The ChPT parameters L_8 , v_{31} and v_{02} in the present study are obtained by requiring that the physical point value $M_\eta = 1103.22$ MeV gets reproduced when the ChPT Eq. (49) and Eq. (50) of the Refs. [63] are used for calculating the m_η and $m_{\eta'}$. The numerical values of the parameters get fixed as the following.

$$L_8 = 1.425 \times 10^{-3}, v_{31} = -0.164 \text{ and } v_{02} = -29.4392 f^2 \quad (40)$$

Note that with the above values of parameters at the physical point, the ChPT expressions in Eqs. (49) and (50) of Ref. [63] give the η and η' masses as $m_\eta = 527.88$ MeV and $m_{\eta'} = 968.73$ which are almost equal to the corresponding masses found in the RQM model. With the above set of $U(3)$ ChPT parameters, the ChPT expressions in the Eqs. (49) and (50) of Ref. [63] give the $m_\eta = 527.34$ MeV and $m_{\eta'} = 977.68$ MeV for the light chiral limit when $m_\pi = 0$ and $m_K = 496$ MeV. The RQM/QM model parameters, for the light

chiral limit, are obtained by using the π, K, η and η' masses as $(m_\pi, m_K, m_\eta, m_{\eta'}) = (0, 496, 527.34, 977.68)$ MeV with the $f_\pi = 90.67$ MeV, $f_K = 113.0216$ MeV and $m_\sigma = 500$ MeV. The QM and RQM model parameters at the physical point and also for the light chiral limit are given in Table II.

III. RESULTS AND DISCUSSION

The temperature variations of the non-strange order parameter in the light chiral limit $m_\pi = 0$ at $\mu = 0$ when $m_\sigma = 500$ MeV for the RQM, Log RPQM and PolyLog-glue RPQM model, are compared in the Fig. 1(a), with the corresponding temperature variations computed in the respective models for the parameters determined at the physical point. The line types for different cases in models are labeled in the Fig. The vertically dropping non-strange order parameter temperature variations, in the light chiral limit signify the second order chiral phase transitions which become crossover transitions for the $m_\pi = 138$ MeV at the physical point in the RQM, Log RPQM and PolyLog-glue RPQM model as the corresponding temperature

TABLE III. Pseudo-critical temperature, Critical temperature for $m_\pi = 0$, Critical end points and Tricritical points.

m_σ	Models	$T_c^\chi(\mu = 0, m_\pi = 138)$ MeV	$T_c(\mu = 0, m_\pi = 0)$ MeV	$(\mu_{\text{CEP}}, T_{\text{CEP}})$ MeV	$(\mu_{\text{TCP}}, T_{\text{TCP}})$ MeV
400	RQM	121.1	122.4	(243.12, 37.03)	(194.6, 65.9)
	QMVT Ref.[118]	144.7	...	(286.0, 32.0)	...
	Log RPQM	146.4	154.4	(230.5, 93.8)	(164.21, 126.41)
	PolyLog-glue RPQM	145.6	149.1	(227.6, 73.6)	(172.4, 107.28)
	RPQM-I	194.1	193.2	(237.8, 104.23)	(168.7, 158.57)
	RPQM-II	172.9	173.4	(228.54, 86.47)	(163.28, 133.47)
	PQMVT-I Ref.[118]	205.0	...	(283.0, 90.0)	...
	PQMVT-II Ref.[118]	205.0	...	(280.0, 83.0)	...
500	QM	129.0	123.2	(165.24, 97.52)	...
	Log PQM	159.3	155.7	(146.6, 124.7)	...
	PolyLog-glue PQM	155.2	150.9	(129.6, 137.7)	...
	RQM	133.6	136.8	(265.42, 38.71)	(220.15, 71.52)
	Log RPQM	148.9	164.5	(252.0, 94.6)	(194.3, 126.53)
	PolyLog-glue RPQM	157.3	160.9	(252.7, 70.9)	(202.20, 108.14)

variations, of the non-strange condensate, develop continuously decreasing tail like structure. The temperature variations of the $\partial x/\partial T$ in the light chiral limit of the RQM, Log RPQM and PolyLog-glue RPQM model when $m_\sigma = 500$ MeV, become divergent and discontinuous in the Fig. 1(b), respectively at the critical temperatures $T_c = 136.8, 164.5$ and 160.9 MeV of the second order chiral phase transitions. The $\partial x/\partial T$ temperature variations for the physical point in the RQM, Log RPQM and PolyLog-glue RPQM model, show a peak respectively at the pseudo-critical temperatures $T_c^\chi = 133.6, 148.9$ and 157.3 MeV [142] of the chiral crossover transitions. Note that the T_c^χ for the crossover transitions in the above models with on-shell renormalized parameters, are smaller than the corresponding critical temperatures T_c of the second order chiral transitions. The temperature axis chiral crossover transitions at $\mu = 0$, occurring respectively at the pseudo-critical temperatures $T_c^\chi = 129.0, 159.3$ and 155.2 MeV in the QM, Log PQM and PolyLog-glue PQM model with the physical point parameters, are significantly sharper because the quark one-loop vacuum correction terms are dropped under the standard mean field approximation (s-MFA) [26, 45, 141, 142]. When parameters in the light chiral limit are used for the $m_\sigma = 500$ MeV, the respective temperature variations of the order parameters at $\mu = 0$ in the QM, Log PQM and PolyLog-glue PQM model under the s-MFA, show a discontinuous jump signifying the first order chiral phase transition (plot not shown in the Fig. 1(a)) respectively at the critical temperatures $T_c = 123.2, 155.7$ and 150.9 MeV (see Table IV). One should note that the theoretical arguments [54], have ruled out any occurrence of a first order chiral phase transition at $\mu = 0$ on the temperature axis, in the light chiral limit of the chiral models. The above mentioned pathology of finding a first order chiral

phase transition on the temperature axis at $\mu = 0$, in the light chiral limit of the QM/PQM model, gets cured when the properly on-shell renormalized quark one-loop vacuum corrections are included in the RQM/RPQM model [141, 142] and one gets a second order chiral phase transition (belonging to the $O(4)$ universality class) in consonance with the prediction of the Ref. [54].

A. Phase diagrams : TCP and CEP

The $2 + 1$ flavor RQM model phase diagrams when $m_\sigma = 400$ and 500 MeV computed for the light chiral limit $m_\pi = 0$ parameters and the physical point $m_\pi = 138$ parameters, are shown in the Fig. 2(a) whereas the $2 + 1$ flavor QM and PolyLog-glue PQM model phase diagrams when $m_\sigma = 500$ MeV computed with the parameters determined at the physical point, are presented in the Fig. 2(b). The line types in the phase diagrams are labeled. The dark red (yellow) color dashed line for the $m_\sigma = 500(400)$ MeV which is the locus of the $O(4)$ critical points for the second order chiral phase transition in the light chiral limit of the RQM model, ends at the tricritical point (TCP) $(\mu_{\text{TCP}}, T_{\text{TCP}}) = (220.15, 71.52)((194.6, 65.9))$ MeV denoted by the solid sky blue triangle (square) and the first order chiral phase transition afterward is denoted by the deep red (yellow) color solid line in the Fig. 2(a). The experimental information for determining the model parameters are available only at the physical point. One needs to know the values of f_π , f_K , m_η , $m_{\eta'}$ when $m_\pi = 0, m_K = 496$ MeV for fixing the model parameters. The above mentioned inputs to find the model parameters in the light chiral limit, are obtained by using the consistent method of large N_c , $U(3)$ chiral perturbation theory which is described briefly in the section II C. For the physical

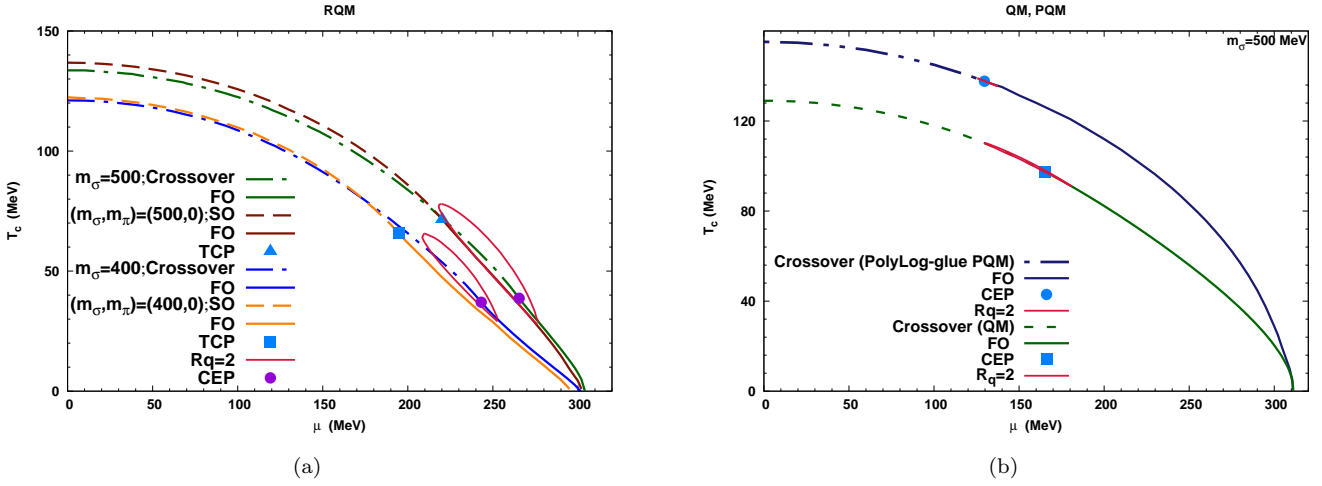


FIG. 2. The RQM model phase diagrams for the $m_\sigma = 400$ and 500 MeV computed for the physical point and light chiral limit parameters, are presented in the left panel (a) while the right panel (b) presents the phase diagrams for the QM model and PolyLog-glue PQM model when the $m_\sigma = 500$ MeV at the physical point. Line types and position of the critical end points (CEP) and tricritical points (TCP) are labeled. The lines enveloping the CEP of different phase diagrams are the contours of constant quark number susceptibility ratio $R_q = 2$.

point parameters in the RQM model, the dark green (blue) dash dot line for the $m_\sigma = 500(400)$ MeV depicting the crossover transition in the Fig. 2(a), ends at the second order critical point of the $Z(2)$ universality class known as the critical end point (CEP). This CEP for the $m_\sigma = 500(400)$ MeV at $(\mu_{\text{CEP}}, T_{\text{CEP}}) = (265.42, 38.71)((243.12, 37.03))$ MeV is denoted by the solid circle in dark violet color and first order transition afterward is shown by the solid line in dark green (blue) color. Since the pseudo-critical (critical) temperature $T_c^\chi(T_c)$ for the crossover (second order) chiral transition occurring at $\mu = 0$ for the $m_\sigma = 400$ MeV is smaller by 12.5 (14.4) MeV than the corresponding $T_c^\chi(T_c)$ for the chiral crossover (second order) transition when the $m_\sigma = 500$ MeV, the phase diagrams for the $m_\sigma = 400$ MeV in the $\mu - T$ plane of the Fig. 2(a), are lying below the corresponding phase diagrams for the $m_\sigma = 500$ MeV.

The CEP in the phase diagram is identified by finding the point in the $\mu - T$ plane at which the quark number susceptibility diverges. The significant enhancement of the quark number susceptibility in the regions of the phase diagram where the CEP lies, can be used as a quantitative measure for mapping the critical regions around the CEP [55–58, 65, 66, 68, 106]. The ratio of the quark number susceptibility computed from the models to the quark number susceptibility obtained from the free quark gas, will be used to quantify the strength of critical fluctuations around the CEP. This ratio represents normalized quark number susceptibility and it is defined as the following.

$$R_q = \frac{\chi_q}{\chi_q^{\text{free}}} \quad (41)$$

The quark number susceptibility is defined as :

$$\chi_q = -\frac{\partial^2 \Omega_{\text{MF}}}{\partial \mu^2} \quad (42)$$

$$\lim_{m_q \rightarrow 0} \chi(T, \mu) = \frac{\nu_q}{6} [T^2 + \frac{3\mu^2}{\pi^2}] = \chi_q^{\text{free}}. \quad (43)$$

Here, $\nu_q = 2N_c N_f$, $N_c = 3$ for three color charges and $N_f = 3$ ($f = u, d, s$) for the 2+1 flavor in the RQM/RPQM model.

The solid line in crimson red color enveloping the CEP for both the $m_\sigma = 500$ and 400 MeV cases of the RQM model in the Fig. 2(a), is the contour of the constant ratio $R_q = 2$ representing the locus of the points in the $\mu - T$ plane, on which the quark number susceptibility is double of the free quark gas susceptibility. The CEP lies higher up on the temperature axis at $(\mu_{\text{CEP}}, T_{\text{CEP}}) = (165.24, 97.52)$ MeV in the phase diagram of the QM model under the s-MFA when $m_\sigma = 500$ MeV in the Fig. 2(b). The constant $R_q = 2$ susceptibility contour for the QM model in the Fig. 2(b), is very small and extremely thin in the temperature direction and it is small in the chemical potential direction also. When compared to the CEP position in the QM model and the critical region around it, the RQM model CEP in the Fig. 2(a), not only shifts to higher μ and lower T (lower right region of the $\mu - T$ plane) due to the effect of quark one-loop vacuum fluctuations but it also has a large, broad and well developed critical region surrounding it. Two different $\mu - T$ planes of the phase diagrams corresponding to the $m_\pi = 0$ and the $m_\pi = 138$ MeV, are plotted in the same two dimensional Fig. 2(a). The three dimensions of the $\mu - T - m_\pi$ coordinates constitute the

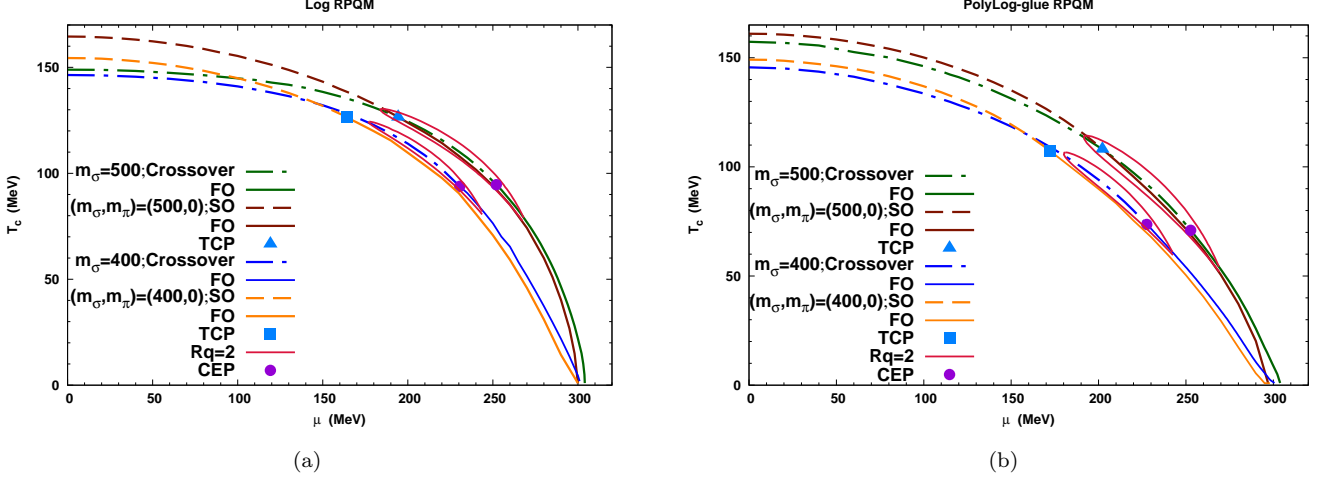


FIG. 3. The phase diagrams for the $m_\sigma = 400$ and 500 MeV computed for the physical point and light chiral limit parameters, are presented in the left panel (a) for the Log RPQM model and right panel (b) for the PolyLog-glue RPQM model. Line types and position of the critical end points (CEP) and tricritical points (TCP) are labeled in the Figs. The lines enveloping the CEP of different phase diagrams are the contours of constant quark number susceptibility ratio $R_q = 2$.

real physical picture. The $R_q = 2$ susceptibility contour in the $\mu - T$ plane for the $m_\pi = 138$ MeV will have its projection (shadow) contour below in the $\mu - T$ plane for the $m_\pi = 0$. The proximity of the TCP from the above mentioned projected contour, would affect the critical fluctuations around the CEP in the $\mu - T$ plane above for the $m_\pi = 138$ MeV. The TCP of the RQM model when $m_\sigma = 500$ MeV, lies on the boundary of the $R_q = 2$ susceptibility contour around the CEP while the TCP for the $m_\sigma = 400$ MeV, gets located noticeably away from the corresponding $R_q = 2$ contour in the Fig. 2(a). It means that the hidden tricritical point would affect the physics of critical fluctuations around the CEP [58, 149] for the case of $m_\sigma = 500$ MeV and this effect will be negligible when the $m_\sigma = 400$ MeV. Polyakov loop potential is known to lift both the $\mu = 0$ chiral crossover transition location and the CEP position, up on the temperature axis in the $\mu - T$ plane when it gets combined with the chiral effective potential of the QM model [45, 142]. For the PolyLog-glue PQM model in the Fig. 2(b), CEP position is significantly up on the temperature axis at $(\mu_{\text{CEP}}, T_{\text{CEP}}) = (137.7, 129.6)$ MeV but the $R_q = 2$ contour around it, is very much pinched and extremely thin similar to what is already reported in the PQM model calculations [117, 118].

In comparison to the RQM model CEP of the Fig. 2(a), the position of CEP for the Log and the PolyLog-glue RPQM model when the $m_\sigma = 500(400)$ MeV, shifts up respectively to the point $(\mu_{\text{CEP}}, T_{\text{CEP}}) = (252.0, 94.6)$ $((230.5, 93.8))$ MeV in the Fig. 3(a) and the point $(\mu_{\text{CEP}}, T_{\text{CEP}}) = (252.7, 70.9) ((227.6, 73.6))$ MeV in the Fig. 3(b). The Polyakov loop potential with no quark back reaction in the Log RPQM model, generates compression in the temperature direction of the critical

region which gets large elongation in the chemical potential direction, therefore the $R_q = 2$ susceptibility contour looks pinched near the CEP in the Fig. 3(a) which is similar to what is found in the Ref. [118]. The critical region is significantly large in the Log RPQM model, but narrower than that of the RQM model in the temperature direction. The Polyakov loop potential caused pinching of the $R_q = 2$ contour near the CEP, becomes small in the Fig. 3(b) due to the smoothing effect of the quark back reaction in the PolyLog-glue RPQM model and one finds a large and broader (somewhat similar to the RQM model) critical region. The above feature gets explained when one notes that the confinement-deconfinement transition gets linked with the chiral phase transitions even at small temperatures and large chemical potentials [48] due to the presence of the quark back reaction in the Polyakov loop potential. It is worth emphasizing that when the $m_\sigma = 500$ MeV for the light chiral limit phase diagram of the PolyLog-glue RPQM model, the position of the tricritical point at $(\mu_{\text{TCP}}, T_{\text{TCP}}) = (202.2, 108.14)$ MeV, gets located well inside the $R_q = 2$ contour in the Fig. 3(b). But for the $m_\sigma = 400$ MeV in the PolyLog-glue RPQM model, the tricritical point at $(\mu_{\text{TCP}}, T_{\text{TCP}}) = (172.4, 107.28)$ MeV gets located well outside the $R_q = 2$ contour. The TCP at $(\mu_{\text{TCP}}, T_{\text{TCP}}) = (194.3, 126.53)$ MeV when the $m_\sigma = 500$ MeV for the light chiral limit phase diagram of the Log RPQM model, also lies well inside the $R_q = 2$ susceptibility contour in the Fig. 3(a) but when the $m_\sigma = 400$ MeV in the Log RPQM model, the TCP at $(\mu_{\text{TCP}}, T_{\text{TCP}}) = (164.21, 126.41)$ MeV, gets located noticeably away from the $R_q = 2$ contour. Thus for the $m_\sigma = 500$ MeV, the critical fluctuations around the CEP will be influenced by the presence of TCP in both the scenarios whether the quark back reaction

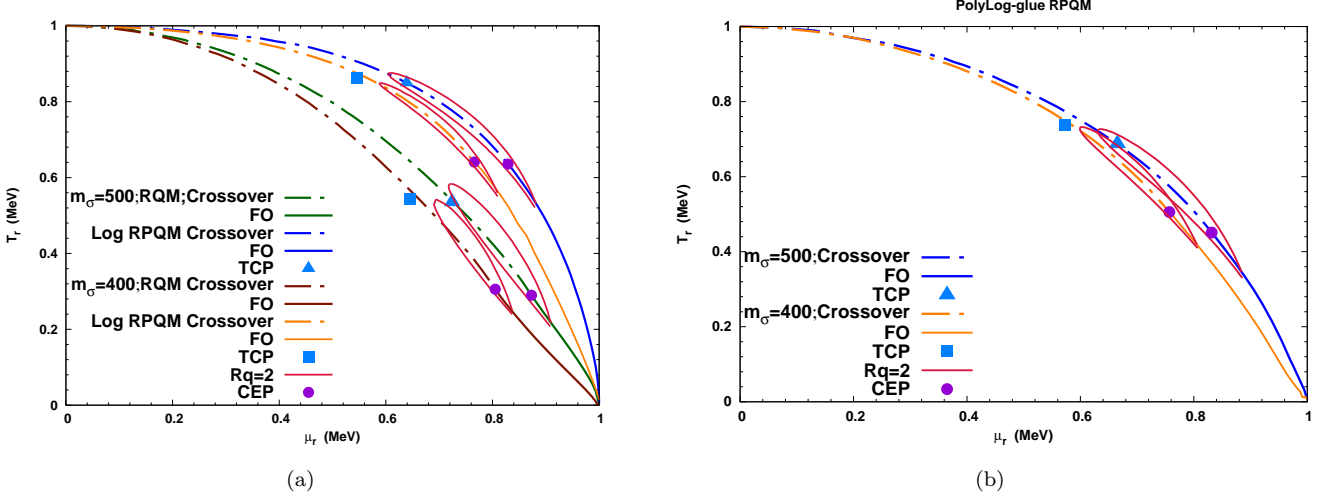


FIG. 4. The phase diagrams for the physical point and light chiral limit parameters when the $m_\sigma = 400$ and 500 MeV are presented in the reduced temperature and chemical potential $\mu_r - T_r$ plane in the left panel (a) for the RQM and Log RPQM model and right panel (b) for the PolyLog-glue RPQM model. Other features of the phase diagrams are same as in the Fig.3. The $T_r = \frac{T}{T_c^\chi}$ is obtained after dividing the temperature T by the pseudo-critical temperature T_c^χ at which the chiral crossover transition occurs on the temperature axis at $\mu = 0$. The $\mu_r = \frac{\mu}{\mu_0}$ is defined after dividing the chemical potential μ by the highest chemical potential μ_0 at which first order chiral phase transition on the μ axis occurs at $T = 0$.

is, absent in the Log RPQM model or present in the PolyLog-glue RPQM model but the influence of TCP would be negligible on the critical fluctuations around the CEP if the $m_\sigma = 400$ MeV in both the versions of the RPQM model as the TCP lies outside of the $R_q = 2$ susceptibility contour.

The comparative effects of different factors, namely 1) the mass of σ meson 2) the quark one-loop vacuum fluctuations 3) Polyakov-loop potential and 4) the presence of quark back reaction in the improved Polyakov loop potential, on the phase diagrams, the CEP and TCP positions and the extent of critical fluctuations around the CEP, are being analyzed in the present work. The larger m_σ , the quark one-loop vacuum fluctuations as well as the Polyakov loop potentials give rise to a different and larger T_c^χ (shown in the Table III) for the temperature axis chiral crossover transition at $\mu = 0$ and the overall phase diagram shifts up in the $\mu - T$ plane [141, 142]. The larger m_σ as well as the effect of quark one-loop vacuum correction cause the CEP position to shift to larger μ and smaller T towards the right in the $\mu - T$ plane of the phase diagram while the different forms of Polyakov loop potentials give rise to differential lifting up of the CEP towards the higher temperatures and lower chemical potentials in the left of the phase diagram [118, 142]. In order to disentangle the effect of different factors, we have plotted the phase diagrams in the reduced temperature T_r and chemical potential μ_r plane of the Fig. 4. Dividing the temperature T by the highest temperature T_c^χ of the chiral crossover transition on the temperature axis at $\mu = 0$, one gets the $T_r = \frac{T}{T_c^\chi}$ and when the chemical potential μ is divided by the highest chemical potential μ_0

at which first order phase transition on the μ axis occurs at $T = 0$, one gets the $\mu_r = \frac{\mu}{\mu_0}$. The curvatures of the crossover and first order transition lines in the Fig. 4(a) and 4(b) become different when the m_σ changes from the 400 to 500 MeV in the RQM/RPQM model. The curvatures change significantly due to the Polyakov loop potential when the quark back reaction is absent in the Log RPQM model in the Fig. 4(a) and the overall phase diagram shifts up with significant bending in the upper right half of the $\mu_r - T_r$ plane. The curvatures of the first order and crossover transition lines in comparison to the corresponding RQM model lines in the Fig. 4(a), show a smooth, uniform and moderate change in the Fig. 4(b) where the quark back reaction is present in the PolyLog-glue form of the Polyakov loop potential and here the overall RPQM Model phase diagram shifts moderately up in the $\mu_r - T_r$ plane.

The CEP at $(\mu_{rCEP}, T_{rCEP}) = (0.80, 0.305)$ and TCP at $(\mu_{rTCP}, T_{rTCP}) = (0.644, 0.544)$ for the case of $m_\sigma = 400$ MeV shift right (higher μ_r and slightly lower T_r) respectively to the CEP at $(\mu_{rCEP}, T_{rCEP}) = (0.87, 0.289)$ and TCP at $(\mu_{rTCP}, T_{rTCP}) = (0.724, 0.535)$ when the σ mass becomes 500 MeV in the RQM model in the Fig. 4(a). The CEP gets significantly lifted up in the Fig. 4(a), due to the Log form of the Polyakov loop potential in the RPQM model, to $(\mu_{rCEP}, T_{rCEP}) = (0.765, 0.640)((0.828, 0.635))$ for the $m_\sigma = 400(500)$ MeV which is more than double of its T_r axis position in the RQM model. The Polyakov loop potential caused lifting up of the TCP to the position $(\mu_{rTCP}, T_{rTCP}) = (0.545, 0.863)((0.639, 0.849))$ for the $m_\sigma = 400(500)$ MeV in the RPQM model is also quite large in the

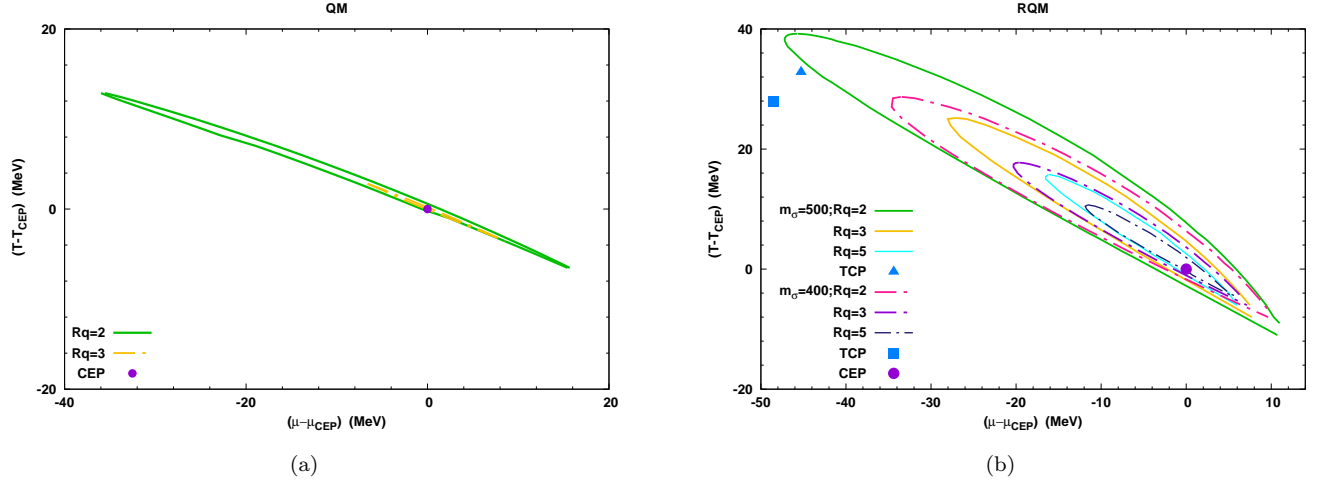


FIG. 5. The $R_q = 2, 3$ susceptibility contours for the QM model are plotted in the left panel (a) while the $R_q = 2, 3, 5$ contours for the RQM model are plotted in the right panel (b).

Fig. 4(a). Owing to the effect of quark back reaction in the PolyLog-glue form of the Polyakov loop potential, the CEP gets a moderate but significant lift up in the Fig. 4(b) to the position $(\mu_{rCEP}, T_{rCEP}) = (0.757, 0.505)((0.831, 0.450))$ for the $m_\sigma = 400(500)$ MeV which is slightly more than one and half times of its T_r axis RQM model position. The TCP for the PolyLog-glue RPQM model in the Fig. 4(b) for the $m_\sigma = 400(500)$ MeV, gets located at the position $(\mu_{rTCP}, T_{rTCP}) = (0.573, 0.682)((0.665, 0.687))$ which is noticeably higher than the TCP position of the RQM model but lower than the position where the Log RPQM model TCP lies in the Fig. 4(a). On comparison with the results obtained for the $m_\sigma = 400$ MeV case, one notes that the the $R_q = 2$ susceptibility contours enveloping the CEP of all the models (RQM, Log RPQM and PolyLog-glue RPQM) when the $m_\sigma = 500$ MeV, have larger spread in both the temperature and chemical potential directions. The earlier conclusion gets reinforced when one notes that the RQM model contours are well rounded and broad (due to the effect of quark one-loop vacuum fluctuation) while the contours get compressed and pinched in the temperature direction due to the Log form of the Polyakov loop potential where quark back reaction is absent in the RPQM model. The pinching in the temperature width of the $R_q = 2$ contours gets significantly moderated by the effect of quark back reaction in the PolyLog-glue form of the Polyakov loop potential and one gets larger and smoother contours (somewhat similar to the RQM model) for the PolyLog-glue RPQM model.

B. Comparing size and shape of critical regions

The susceptibility contours corresponding to three different constant ratios $R_q = 2, 3$ and 5, have been plotted

for the relevant range of temperatures and chemical potentials in the Fig. 5 and Fig. 6 for analyzing the size and shape of the critical regions surrounding the CEP of the QM, RQM, Log RPQM and PolyLog-glue RPQM model. The extent of QM model $R_q = 2$ contour in the Fig. 5(a) is 19.4 MeV in the temperature direction (12.9 MeV above and 6.5 MeV below the T_{CEP} on the T axis) and 51.3 MeV in the chemical potential direction (35.9 MeV lower and 15.4 MeV higher than the μ_{CEP} on the μ axis). For the $R_q = 3$ contour of the QM model, the size is very small as its T axis spread is only 6.3 MeV (2.8 MeV above and 3.5 MeV below the T_{CEP}) whereas the μ axis spread is only 15 MeV (6.6 MeV lower and 8.4 MeV higher than the μ_{CEP}). The critical region around the CEP of QM model is quite small and very much compressed in the temperature direction.

The $R_q = 2$ contour of the RQM model when the $m_\sigma = 500(400)$ MeV in the Fig. 5(b), is spread to 50.2 (36.7) MeV {39.2(28.7) MeV above and 11(8) MeV below the T_{CEP} } on the T axis while the corresponding spread on the μ axis is 58.3(44.3) MeV {47.2(34.6) MeV lower and 11.1(9.7) MeV higher than the μ_{CEP} }. The smaller size of the $R_q = 3$ contour for the $m_\sigma = 500(400)$ MeV is 33.2(25.1) MeV on the T axis {25.2(17.7) MeV above and 8(7.4) MeV below the T_{CEP} } and 35.7(29.7) MeV on the μ axis {28(20.3) MeV lower and 7.7(9.4) MeV higher than the μ_{CEP} }. The smallest spread of the $R_q = 5$ contour corresponding to the $m_\sigma = 500(400)$ MeV, is 21.8(15.2) MeV on the T axis {15.8(10.7) MeV above and 6(4.5) MeV below the T_{CEP} } and 22.4(17.7) MeV on the μ axis {16.5(11.9) MeV lower and 5.9(5.8) MeV higher than the μ_{CEP} }. The extensions of the $R_q = 2, 3$ and 5 contours for the $m_\sigma = 400$ MeV along the T axis and μ axis in the Fig. 5(b), are smaller than the corresponding contour sizes for the $m_\sigma = 500$ MeV in the sequential order of (13.5, 8.1 and 6.6) MeV on the T axis and (14.0, 6.0 and 4.7) MeV on the μ axis. One can see that the spreads of

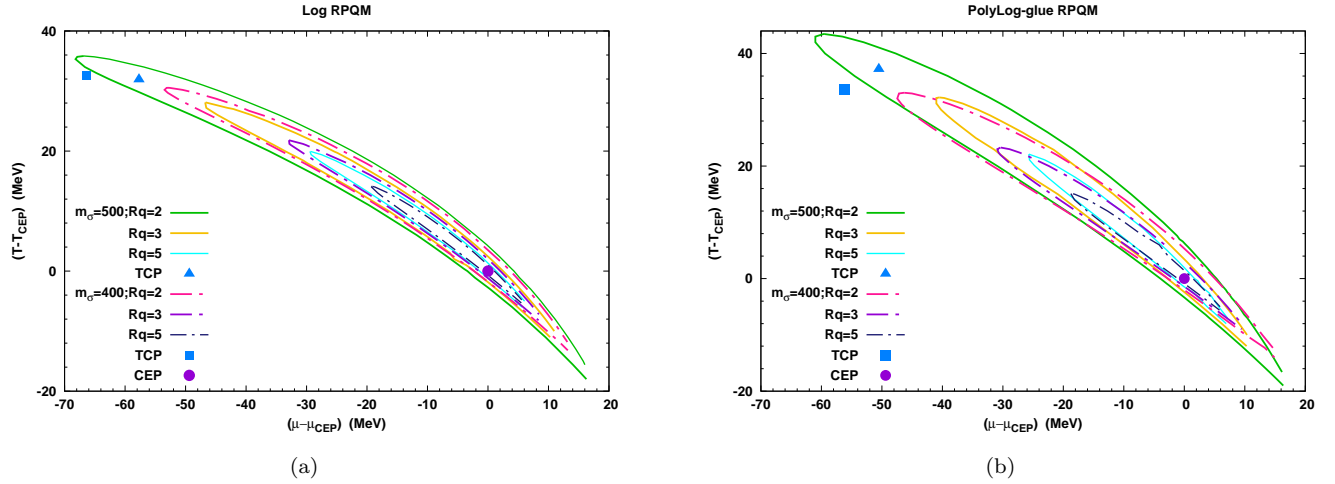


FIG. 6. The $R_q = 2, 3, 5$ susceptibility contours are plotted in the left panel (a) for the Log RPQM model while the right panel (b) presents the contour plots for the PolyLog-glue RPQM model.

the RQM model susceptibility contours in the temperature direction are nearly equivalent to their spread in the chemical potential direction (only the $R_q = 2$ contour is about 14 percent larger along the μ axis (by 8 MeV) when compared to its size along the T axis). It is worth pointing out that the consistently treated effect of the quark one-loop vacuum fluctuations in the improved effective potential of the RQM model, gives rise to a broad, somewhat symmetrical critical regions enveloping the CEP, which are larger in a direction perpendicular to the crossover transition line. Furthermore when the $m_\sigma = 500$ MeV in the RQM model, the TCP lies very close to the boundary of the outer $R_q = 2$ contour while the TCP lies significantly away from the boundary of the $R_q = 2$ contour when the $m_\sigma = 400$ MeV.

In the Fig. 6(a), the Log RPQM model $R_q = 2$ contour for the $m_\sigma = 500(400)$ MeV is extended to 53.8 (43.7) MeV on the T axis {35.8(30.5) MeV above and 18(13.2) MeV below the T_{CEP} } and 84.5 (66.3) MeV on the μ axis {68.20(53.1) MeV lower and 16.3(13.2) MeV higher than the μ_{CEP} }. The smaller size of $R_q = 3$ contour for the $m_\sigma = 500(400)$ MeV is extended to 39.1(30) MeV on the T axis {28.1(21.8) MeV above and 11(8.2) MeV below the T_{CEP} } and 57.6(41.3) MeV on the μ axis {46.7(32.9) MeV lower and 10.9(8.4) MeV higher than the μ_{CEP} }. The extent of smallest $R_q = 5$ contour when the $m_\sigma = 500(400)$ MeV, is 25.9 (19.6) MeV on the T axis {19.9(14.1) MeV above and 6(5.5) MeV below the T_{CEP} } and 35.4 (24.8) MeV on the μ axis {29.4(19.2) MeV lower and 6.0(5.6) MeV higher than the μ_{CEP} }. The T axis and μ axis extensions of the $R_q = 2, 3$ and 5 contours in the Fig. 6(a) for the $m_\sigma = 400$ MeV, are smaller than the corresponding contour sizes for the $m_\sigma = 500$ MeV in the sequential order of (10.1, 9.1 and 6.3) MeV on the T axis and (18.2, 16.2 and 10.6) MeV on the μ axis. The chemical potential direction stretching of the Log RPQM model $R_q = 2, 3$ and 5 contours for the $m_\sigma = 500(400)$

MeV, are noticeably larger than their respective extension in the temperature direction respectively by a factor of 1.57 (1.52), 1.47 (1.38) and 1.37 (1.27). The smoothing effect of quark one-loop vacuum fluctuation that generates broader and larger critical region perpendicular to the crossover transition line in the RQM model, looks somewhat compromised in the presence of Log Polyakov loop potential and one finds that the width of contours near the CEP, become narrow owing to its compression in the temperature direction similar to what is noticed in the Ref. [118]. Note that when the $m_\sigma = 400$ MeV in the Log RPQM model, the TCP lies noticeably away from the boundary of the $R_q = 2$ contour whereas the TCP lies inside the $R_q = 2$ contour for the $m_\sigma = 500$ MeV.

The spread of the PolyLog-glue RPQM model $R_q = 2$ contour in the Fig. 6(b) for the $m_\sigma = 500(400)$ MeV is 62.4 (47) MeV on the T axis {43.4(33) MeV above and 19(14) MeV below the T_{CEP} } and 77.4 (62.4) MeV on the μ axis {61.0(47.5) MeV lower and 16.4(14.9) MeV higher than the μ_{CEP} }. The smaller size of the $R_q = 3$ contour for the $m_\sigma = 500(400)$ MeV, is spread 44.2(32.3) MeV on the T axis {32.2(23.3) MeV above and 12(9) MeV below the T_{CEP} } and 51.4(40.4) MeV on the μ axis {41.0(30.9) MeV lower and 10.4(9.5) MeV higher than the μ_{CEP} }. The smallest spread of the $R_q = 5$ contour for the $m_\sigma = 500(400)$ MeV is 30.1 (20.7) MeV on the T axis {22.1(15.1) MeV above and 8(5.6) MeV below the T_{CEP} } and 32.8 (24.6) MeV on the μ axis {25.7(18.7) MeV lower and 7.1(5.9) MeV higher than the μ_{CEP} }. The T axis and μ axis extensions of the $R_q = 2, 3$ and 5 contours for the $m_\sigma = 400$ MeV in the Fig. 6(b), are smaller than the corresponding contour sizes for the $m_\sigma = 500$ MeV in the sequential order of (15.4, 11.9 and 9.4) MeV on the T axis and (15, 11 and 8.2) MeV on the μ axis. The stretching of the $R_q = 2, 3$ and 5 contours for the $m_\sigma = 500(400)$ MeV in the chemical potential direction for the PolyLog-glue RPQM model, are moderately larger than their respec-

TABLE IV. The T and μ axis spread of the $R_q = 2, 3$ and 5 contours in different model scenarios. The size of the contours above and below T_{CEP} are denoted respectively by the ΔT_a and ΔT_b while the total contour size on T axis is ΔT . The size of the contours on the lower side and higher side of the μ_{CEP} are denoted respectively by the $\Delta \mu_l$ and $\Delta \mu_h$ while the total contour size on μ axis is $\Delta \mu$.

Models	Entries below the ΔT_a , ΔT_b , ΔT , $\Delta \mu_l$, $\Delta \mu_h$ and $\Delta \mu$ correspond to the susceptibility ratio $\mathbf{R}_q = 2(3)(5)$					
	ΔT_a	ΔT_b	$\Delta T = \Delta T_a + \Delta T_b$	$\Delta \mu_l$	$\Delta \mu_h$	$\Delta \mu = \Delta \mu_l + \Delta \mu_h$
RQM ($m_\sigma = 400$)	28.7(17.7)(10.7)	8.0(7.4)(4.5)	36.7(25.1)(15.2)	34.6(20.3)(11.9)	9.74(9.4)(5.8)	44.3(29.7)(17.7)
QMVT Ref.[118]	31.4(19.5)(11.5)	16.0(7.7)(4.1)	47.4(27.2)(15.6)	32.8(17.6)(9.1)	10.1(6.3)(3.3)	42.9(23.9)(12.4)
Log RPQM	30.5(21.8)(14.1)	13.2(8.2)(5.5)	43.7(30.0)(19.6)	53.1(32.9)(19.2)	13.2(8.4)(5.6)	66.3(41.3)(24.8)
PolyLog-glue RPQM	33.0(23.3)(15.1)	14.0(9.0)(5.6)	47.0(32.3)(20.7)	47.5(30.9)(18.7)	14.9(9.5)(5.9)	62.4(40.4)(24.6)
RPQM-I	32.1(23.0)(15.4)	14.2(9.0)(6.0)	46.3(32.0)(21.4)	27.5(18.1)(11.4)	8.9(5.6)(3.5)	36.4(23.7)(14.9)
RPQM-II	37.1(26.5)(17.4)	16.0(10.0)(6.5)	53.1(36.5)(23.9)	41.0(27.3)(16.7)	13.2(8.3)(5.2)	54.2(35.6)(21.9)
PQMVT-I Ref.[118]	49.8(33.9)(20.7)	41.1(21.7)(11.2)	90.9(55.6)(31.9)	33.6(19.5)(11.1)	12.6(7.9)(4.4)	46.2(27.4)(15.5)
PQMVT-II Ref.[118]	49.9(33.9)(20.3)	36.5(19.8)(8.8)	86.4(53.7)(29.1)	48.6(27.5)(14.8)	15.4(10.0)(5.5)	64.1(37.5)(20.3)
QM ($m_\sigma = 500$)	12.9(2.8)	6.5(3.5)	19.4(6.3)	35.9(6.6)	15.4(8.4)	51.3(15.0)
RQM	39.2(25.2)(15.8)	11.0(8.0)(6.0)	50.2(33.2)(21.8)	47.2(28.0)(16.5)	11.1(7.7)(5.9)	58.3(35.7)(22.4)
Log RPQM	35.8(28.1)(19.9)	18.0(11.0)(6.0)	53.8(39.1)(25.9)	68.2(46.7)(29.4)	16.3(10.9)(6.0)	84.5(57.6)(35.4)
PolyLog-glue RPQM	43.4(32.2)(22.1)	19.0(12.0)(8.0)	62.4(44.2)(30.1)	61.0(41.0)(25.7)	16.4(10.4)(7.1)	77.4(51.4)(32.8)

tive extension in the temperature direction respectively by a factor of 1.24 (1.33), 1.16 (1.25) and 1.09 (1.19). We point out that the effect of quark back reaction in the PolyLog-glue RPQM model, causes smaller stretching of the contours in the chemical potential direction whereas the temperature direction stretching becomes larger in a similar proportion when the results are compared with the corresponding stretching of the contours noticed in the Fig. 6(a) for the Log RPQM model. Thus the temperature direction compression in the width of the contours near the CEP becomes small due to the smoothing effect of the quark back reaction in the PolyLog-glue model where contours are noticeably broader than the corresponding Log RPQM model contours. In the PolyLog-glue RPQM model also, the TCP lies away from the boundary of the $R_q = 2$ contour when the $m_\sigma = 400$ MeV while the TCP lies quite well inside the $R_q = 2$ contour when the $m_\sigma = 500$ MeV.

C. Comparing RQM model critical regions with results of Ref.[118]

Recall that after adding the quark one-loop vacuum fluctuations to the effective potential of the QM model, several studies [115–118] have used the curvature masses of the mesons to fix the model parameters. Since the curvature masses incorporate the quark one-loop vacuum corrections in the meson self energies only at the zero momentum, the curvature mass based parameter fixing become inconsistent in the above studies of the quark meson/Polyakov quark meson with the vacuum term (QMVT/PQMVT) model. Recent two and 2+1 flavor RQM/RPQM model studies [139–142] with the consistent on-shell renormalized parameters, have shown that the calculated shift, in the position of the CEP to

the lower right corner in the $\mu - T$ plane of the phase diagram, is quite large due to the overestimation of the effect of quark one-loop corrections in the above mentioned QMVT/PQMVT model studies. Therefore it is important to compare below the earlier reported shape and size of the critical regions around the CEP in the 2+1 flavor curvature mass parametrized QMVT/PQMVT model study of the Schaefer et.al. [118], with the spread of the critical regions around the CEP of the 2+1 flavor RQM/RPQM model in the present work when the $m_\sigma = 400$ MeV and the Log form of Polyakov-loop potential is considered with the $T_0 = 270$ MeV for the Pure Yang-Mills $SU_c(3)$ gauge theory. The critical regions around the CEP of the QMVT and RQM will be compared first in the following.

The $R_q = 2$ susceptibility contour in the Fig.3(b) of the Ref. [118] (after extracting the data) for the QMVT model is extended around its CEP at $(\mu_{\text{CEP}}, T_{\text{CEP}}) = (286, 32)$ MeV, to about 31.3 MeV above and 16 MeV below the T_{CEP} on the T axis while the spread of the contour on the μ axis is 32.8 MeV to the lower left and 10.1 MeV to the higher right side of the μ_{CEP} . In contrast to the above, the CEP in our RQM model work is positioned higher up and noticeably left at the $(\mu_{\text{CEP}}, T_{\text{CEP}}) = (243.12, 37.03)$ MeV around which the $R_q = 2$ contour (in the Fig. 5(b) for the $m_\sigma = 400$ MeV) is extended on the T axis to 28.7 MeV above and 8 MeV below the T_{CEP} while its μ axis spread is 34.6 MeV on the lower left and 9.7 MeV on the higher right side of the μ_{CEP} . The total size of 36.7 MeV of the RQM model contour on the T axis, is smaller than the total T axis size of 47.3 MeV for the QMVT model contour whereas the RQM model contour total μ axis size of 44.3 MeV, is larger than the total size of 42.9 MeV on the μ axis for the QMVT model. Note that, on the lower side of its T_{CEP} on the T axis in the Fig.3(b) of Ref. [118], the QMVT model

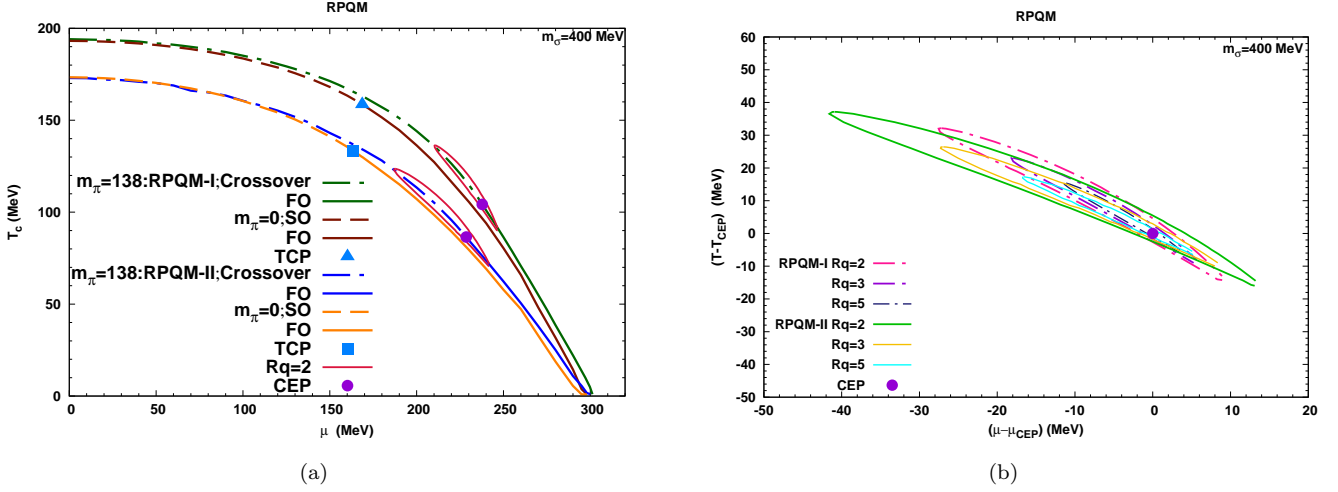


FIG. 7. The RPQM-I and RPQM-II model phase diagrams for the light chiral limit and physical point parameters are presented in the left panel (a) while the contours for the constant susceptibility ratio $R_q = 2, 3$ and 5 are presented in the right panel (b). The Log RPQM model in the present work with the $T_0 = 270$ MeV, $m_\sigma = 400$ MeV and no quark back reaction, is termed as the RPQM-I model. The PolyLog-glue RPQM model with the quark back reaction where the $T_0 = 270$ MeV and $m_\sigma = 400$ MeV, has been termed as the RPQM-II model

$R_q = 2$ contour is 8 MeV larger in size than the size of the RQM model $R_q = 2$ contour on the lower side of its T_{CEP} on the T axis in the Fig. 5(b) while on the upper side of its T_{CEP} , the QMVT model $R_q = 2$ contour is only 2.6 MeV larger than the size of the RQM model $R_q = 2$ contour that lies above its T_{CEP} in the Fig. 5(b). The shape of the QMVT model contour has a neck like narrow bending structure below its T_{CEP} because the curvature of the first order transition line below the CEP $(\mu_{\text{CEP}}, T_{\text{CEP}}) = (286, 32)$ MeV is large, in the Fig. 3(b) of Ref. [118], as the 32 MeV of temperature has to decrease to $T \simeq 0$ in the span of the chemical potential difference $(\mu_0 - \mu_{\text{CEP}}) = 300.13 - 286 = 14.13$ MeV when the first order transition line hits the highest $\mu_0 = 300.13$ MeV when $T \simeq 0$ on the chemical potential axis. In contrast to the above the RQM model contour looks smooth and more symmetrical where narrow bending is absent below its T_{CEP} because the curvature of the first order transition line below the CEP $(\mu_{\text{CEP}}, T_{\text{CEP}}) = (243.12, 37.03)$ MeV is noticeably smaller, in the Fig. 2(a), as the 37 MeV of temperature has to decrease to $T \simeq 0$ in a significantly larger span of the chemical potential difference $(\mu_0 - \mu_{\text{CEP}}) = 302 - 243 \simeq 59$ MeV when the first order transition line hits the highest $\mu_0 = 302$ MeV when $T \simeq 0$ on the chemical potential axis.

Furthermore the RQM model contour closes at $(\mu, T) = (208.52, 65.73)$ MeV on the upper left side and $(\mu, T) = (252.82, 29.03)$ MeV on the lower right side while the QMVT model contour closes at $(\mu, T) = (253.2, 63.4)$ MeV on the upper left and at $(\mu, T) = (296.1, 16.0)$ MeV on the lower right side. Note that the complete RQM model phase diagram in the $\mu - T$ plane of the Fig. 2(a) for the $m_\sigma = 400$ MeV, would lie below the QMVT model phase diagram in the Fig. 1(b) of the Ref. [118] as the

$(\mu_0, T_c^\chi) = (302, 121.1)$ MeV in the RQM model while the $(\mu_0, T_c^\chi) = (300.13, 144.1)$ MeV in the QMVT model. Recall that the T_c^χ is the pseudo-critical temperature of the chiral crossover transition occurring on the temperature axis at $\mu = 0$ while the μ_0 is the highest chemical potential at which the first order chiral transition occurs for the $T \simeq 0$. In order to see the real difference between the size and shape of the critical regions for the RQM and QMVT model, one has to compare the quantities in terms of the reduced chemical potential $\mu_r = \frac{\mu}{\mu_0}$ and temperature $T_r = \frac{T}{T_c^\chi}$. In terms of the reduced variables, the RQM and QMVT model $R_q = 2$ contour closes respectively at $(\mu_r, T_r) = (0.6904, 0.5425)$ and $(\mu_r, T_r) = (0.8436, 0.440)$ on the upper left side while on the lower right side of the phase diagram, the RQM and QMVT model contour closes respectively at $(\mu_r, T_r) = (0.837, 0.239)$ and $(\mu_r, T_r) = (0.9865, 0.111)$. Note also that the RQM and QMVT model CEP lies respectively at $(\mu_{r\text{CEP}}, T_{r\text{CEP}}) = (0.805, 0.306)$ and $(\mu_{r\text{CEP}}, T_{r\text{CEP}}) = (0.9529, 0.2268)$.

The model setting of the Log form of the Polyakov-loop potential with constant $T_0 = 270$ MeV for the Pure Yang-Mills $SU_c(3)$ gauge theory in the work of Schaefer et.al., has been termed as the PQMVT-I for the purpose of comparison while their scenario with the quark matter back reaction in the Log Polyakov-loop potential, is termed as the PQMVT-II where the $T_0(\mu)$ is chemical potential dependent. For comparison with the work of Ref. [118], the Log RPQM model in our work with the $T_0 = 270$ MeV, $m_\sigma = 400$ MeV and no quark back reaction, has been termed as the RPQM-I model. The enhancement of the RQM model with the improved PolyLog-glue form of the Polyakov loop potential [46–48], accounts for the quark back reaction in our work where this model setting with the param-

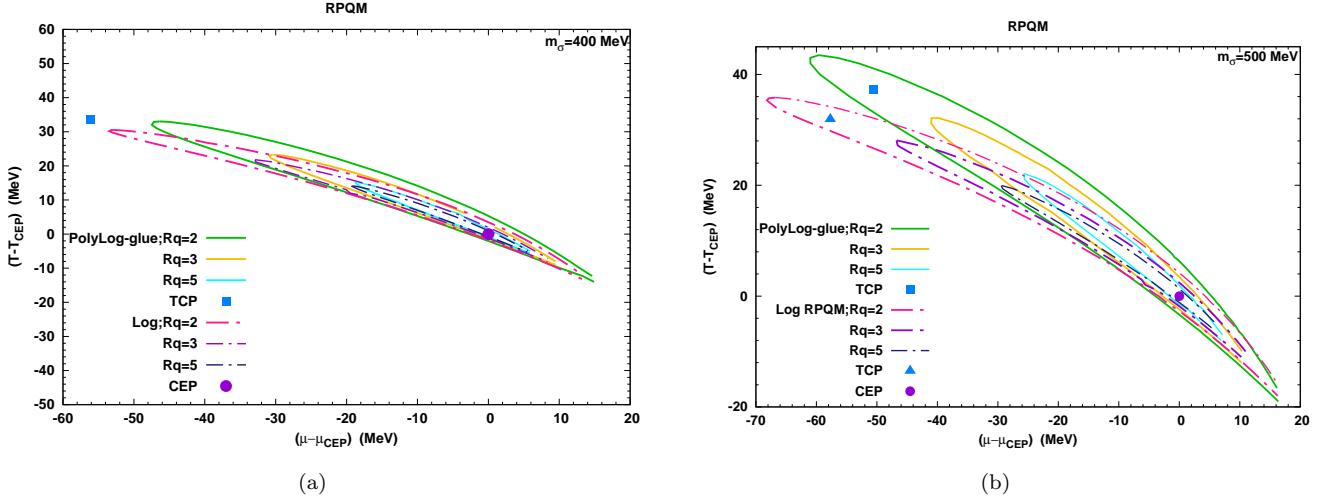


FIG. 8. With the $T_0 = T_c^{glue} = 187$ MeV for the Polyakov loop potentials in the Log and PolyLog-glue RPQM model, the $R_q = 2, 3, 5$ susceptibility contours are presented in the left panel (a) for the case of $m_\sigma = 400$ MeV and right panel (b) for the case of $m_\sigma = 500$ MeV

ter $T_c^{glue} = T_0 = 270$ MeV, has been termed as the RPQM-II model. The CEP in our RPQM-I (RPQM-II) model work without (with) quark back reaction in the Fig.7(a) gets located significantly left and noticeably higher up in the phase diagram at the $(\mu_{CEP}, T_{CEP}) = (237.8(228.54), 104.23(86.47))$ MeV when it is compared with the PQMVT-I (PQMVT-II) model CEP without (with) quark back reaction lying at the $(\mu_{CEP}, T_{CEP}) = (283(280), 90(83))$ MeV in the Fig.1(b) of Ref. [118].

After extracting the data from the Fig.3(a) of the Ref. [118], one finds that the $R_q = 2$ susceptibility contour for the PQMVT-I (PQMVT-II) model is extended around its CEP on the T axis to about 49.81 (49.96) MeV above and 41.13 (36.48) MeV below the T_{CEP} while the spread of the contour on the μ axis is 33.63 (48.61) MeV to the lower left and 12.56 (15.45) MeV to the higher right side of the μ_{CEP} . In contrast to the above, the Fig. 7(b) of the present work shows that the RPQM-I (RPQM-II) model susceptibility $R_q = 2$ contour is extended on the T axis to 32.1 (37.1) MeV above and 14.2 (16) MeV below the T_{CEP} while its μ axis spread is 27.5 (41) MeV on the lower left and 8.9 (13.2) MeV on the higher right side of the μ_{CEP} . The total T axis size of the RPQM-I (RPQM-II) model contour of 46.3 (53.1) MeV, is significantly smaller than the total size of 90.94 (86.44) MeV on the T axis for the corresponding $R_q = 2$ PQMVT-I (PQMVT-II) model contour while the total μ axis size of the RPQM-I (RPQM-II) model contour of 36.4 (54.2) MeV, is only about 10 MeV smaller than the total size of 46.19 (64.06) MeV on the μ axis for the PQMVT-I (PQMVT-II) model contour. The reason of the above difference is the fact that the RPQM-I (RPQM-II) model critical regions are centered around a CEP which lies at significantly smaller chemical potentials $\mu_{CEP} = 237.8(228.54)$ MeV in the phase diagram while temperatures are moderately larger

at $\mu_{CEP} = 104.23(86.47)$. Furthermore, to have a proper perspective of the above difference, one should also note that the $T_c^X = 194.1$ MeV at the $\mu = 0$ for the RPQM-I model phase diagram in the Fig. 7(a) and its CEP lies significantly up (higher T) towards the left (lower μ) when compared to the position of the CEP in the Fig.1(b) for the PQMVT-I model phase diagram where $T_c^X = 205$ MeV at the $\mu = 0$. The detailed comparative analysis for different model settings has been done only for the $R_q = 2$ contour. One can see a similar pattern of comparative differences for the $R_q = 3$ and 5 contours in different model scenarios by looking at the Table (IV).

The total size of 90.94 MeV on the T axis (with large stretching of 41.1 MeV below the T_{CEP}) for the PQMVT-I model contour with no quark back reaction, is almost double of its μ axis total size of 46.19 MeV and the width of contour gets successively narrower and more compressed in the temperature direction as one goes below the CEP in the Fig.3(a) of Ref. [118]. In comparison to the QMVT model, the significantly enhanced critical region with a relatively compressed width for the PQMVT-I model was attributed to the observations that the 1) Polyakov loop modifies the quark determinant mostly at moderate chemical potentials and 2) PQMVT model CEP is placed at significantly higher $T_{CEP} = 90$ MeV whereas the CEP in both the QMVT and PQMVT models gets located at larger chemical potentials around 280–285 MeV [118]. The PQMVT model contour of a successively decreasing width below its T_{CEP} , has a larger neck like narrow structure because the curvature of the first order transition line below the CEP $(\mu_{CEP}, T_{CEP}) = (283, 90)$ MeV is quite large, in the Fig.3(a) of Ref. [118], as the 90 MeV of large temperature has to decreases to $T \simeq 0$ in the span of the chemical potential difference of only $(\mu_0 - \mu_{CEP}) = 299.54 - 283 = 16.54$ MeV when the first order transition line hits the highest

$\mu_0 = 299.56$ MeV when $T \simeq 0$ on the chemical potential axis. Note that since the total T axis contour size of the 46.3 MeV, is only 9.9 MeV larger than the μ axis total contour size of 36.4 MeV, the RPQM-I model $R_q = 2$ contour (for no quark back reaction) looks more symmetrical, smoother and its narrowing below the CEP is quite small in the Fig. 7(b) when one compares it with the RQM model $R_q = 2$ contour for the $m_\sigma = 400$ MeV in the Fig. 5(b). In contrast to the PQMVT-I model contour also, the RPQM-I model contour being significantly smaller in the T direction, looks smooth and more symmetrical where narrow bending is absent below its T_{CEP} because the curvature of the first order transition line below the CEP $(\mu_{\text{CEP}}, T_{\text{CEP}}) = (237.8, 104.23)$ MeV is noticeably smaller, in the Fig. 7(a), as about the 104 MeV of temperature (though large) has to decrease to $T \simeq 0$ in a significantly larger span of the chemical potential difference $(\mu_0 - \mu_{\text{CEP}}) = 301.2 - 237.8 \simeq 63.4$ MeV when the first order transition line hits the highest $\mu_0 = 301.2$ MeV when $T \simeq 0$ on the chemical potential axis.

The presence of differently treated quark back reaction in the PolyLog-glue Polyakov loop potential, causes significant smoothing effect in the RPQM-II model because the total T axis size of 53.1 MeV for the $R_q = 2$ contour, is almost equal to its total μ axis size of 54.2 MeV in the Fig. 7(b) and the overall contour looks quite symmetrical and smooth where narrowing below the CEP disappears. In contrast to the above, the Ref. [118] has taken μ dependence of T_0 to account for the quark back reaction in the PQMVT-II model where the T axis total size of 86.44 MeV (with still a large stretching of 36.48 MeV below the T_{CEP}) for the $R_q = 2$ contour, is about 1.35 times of its μ axis total size of 64.06 MeV. The width of the PQMVT-II model contour also gets successively more compressed below its CEP similar to the case of the PQMVT-I model but the narrowing in the contour shape, is smaller than what is noticed for the PQMVT-I model. Note that in the PQMVT-II model $T_c^\chi = 205$ MeV at the $\mu = 0$ is same as in the PQMVT-I model with no quark back reaction.

The RPQM-I (RPQM-II) model $R_q = 2$ contour closes at $(\mu, T) = (210.3(187.54), 136.33(123.57))$ MeV on the upper left side and $(\mu, T) = (246.7(241.74), 90.03(70.47))$ MeV on the lower right side while the PQMVT-I(PQMVT-II) model $R_q = 2$ contour closes at $(\mu, T) = (249.37(231.39), 139.81(129.96))$ MeV on the upper left and at $(\mu, T) = (295.56(295.45), 48.87(43.52))$ MeV on the lower right side. Note that the complete RPQM-I(RPQM-II) model phase diagram for the $m_\sigma = 400$ MeV in the $\mu - T$ plane of the Fig. 7(a), would lie below the PQMVT-I(PQMVT-II) model phase diagram in the Fig.1(b) of the Ref. [118] as the $(\mu_0, T_c^\chi) = (301.2(300.0), 194.1(179.2))$ MeV in the RPQM-I(RPQM-II) model while the $(\mu_0, T_c^\chi) = (299.54(299.54), 205(205))$ MeV in the PQMVT-I(PQMVT-II) model. Comparing the quantities in terms of the reduced chemical potential μ_r and temperature T_r , one can see the real difference

between the size and shape of the critical regions for the RPQM-I (RPQM-II) and PQMVT-I(PQMVT-II) model. In terms of the reduced variables, the RPQM-I(RPQM-II) model and PQMVT-I(PQMVT-II) model $R_q = 2$ contours close respectively at the $(\mu_r, T_r) = (0.6982(0.625), 0.7023(0.714))$ and $(\mu_r, T_r) = (0.832(0.772), 0.682(0.633))$ on the upper left side while on the lower right side of the phase diagram, the RPQM-I(RPQM-II) and PQMVT-I(PQMVT-II) model contours close respectively at the $(\mu_r, T_r) = (0.819(0.805), 0.4638(0.407))$ and $(\mu_r, T_r) = (0.986(0.986), 0.238(0.212))$. Here one should also take note of the position of CEP for the RPQM-I(RPQM-II) model and PQMVT-I(PQMVT-II) model in terms of reduced variables respectively at $(\mu_{r\text{CEP}}, T_{r\text{CEP}}) = (0.7895(0.761), 0.5369(0.5))$ and $(\mu_{r\text{CEP}}, T_{r\text{CEP}}) = (0.944(0.934), 0.439(0.404))$.

Note that the temperature direction positions of the PolyLog-glue RPQM-II model contours (with quark back reaction) though having larger T and μ axis spread, lie below the Log RPQM-I model contours which have smaller spread in the Fig. 7(b). The PQMVT-II model contours with quark back reaction lying below the PQMVT-I model contours (though their spread is a bit larger on the T axis) have similar temperature direction ordering of positions in the Fig.3(a) of Ref. [118]. But the above ordering of position in the temperature direction, gets reversed in the Fig. 8(a) when T_0 is 187 MeV in the Polyakov loop potentials for the 2+1 flavor of dynamical quarks and here the Log RPQM model contours with no quark back reaction lie below the PolyLog-glue RPQM model contours in the temperature direction. The Log RPQM model contours have larger μ axis and slightly smaller T axis spread when compared with the contours of PolyLog-glue model. The above features for the Log RPQM model and PolyLog-glue RPQM model get enhanced for the case of $m_\sigma = 500$ MeV in the Fig. 8(b).

IV. SUMMARY

The consistently treated, quark one-loop vacuum fluctuations and proper renormalization of the parameters in the renormalized quark meson (RQM) model by matching the counter terms in the on-shell scheme with those in the modified minimal subtraction $\overline{\text{MS}}$ scheme, give rise to significantly stronger 't Hooft coupling c and weaker explicit chiral symmetry breaking strength h_x and h_y . The critical end point (CEP), gets upward lift in the phase diagram of the RQM model [141, 142] due to the above novel features and this upward jump of the CEP becomes significant in the phase diagram of the renormalized Polyakov quark meson (RPQM) model when Polyakov loop potential with or without quark back reaction gets added to the effective potential of the RQM model. Placed higher up in the $\mu - T$ plane than the location of the CEP computed in the phase diagram of the curvature mass based parametrized Polyakov quark

meson model with vacuum term (called the PQMVT model) study in the Ref. [118], the CEP in the RPQM model [142], lies closer to the estimated range of critical point positions in the QCD phase diagram : $T_c \sim (100 - 110)$ MeV and $\mu_B \sim (420 - 650) \Leftrightarrow \mu_{\text{CEP}} \sim (140 - 217)$ MeV given by the most recent results of different theoretical techniques [74]. Therefore the mapping of the critical regions around the CEP of the RQM and RPQM model becomes important.

The temperature variations of the order parameter and its temperature derivative were computed for the light chiral limit $m_\pi = 0$ of the RQM/RPQM model when the $m_\sigma = 500$ MeV to find the critical temperature T_c of second order chiral phase transition occurring at $\mu = 0$. The PolyLog-glue and Log form of the Polyakov loop potentials with and without quark back reactions in respective order were used in the RPQM model. The changed values of f_π , f_K , m_η and $m_{\eta'}$ required for finding the RQM model parameters in the light chiral limit $(m_\pi, m_K) = (0, 496)$ MeV were determined using the large N_c standard chiral perturbation theory inputs from the Refs. [61–63]. Serving the first objective of the present work, the light chiral limit phase diagrams of the RQM model, Log RPQM and PolyLog-glue RPQM model (where parameter $T_0 = T_c^{\text{glue}} = 187$ MeV for the 2+1 flavor of dynamical quarks in the Polyakov loop potential), are computed for two different $m_\sigma = 400$ and 500 MeV. These phase diagrams are compared with the corresponding model phase diagrams [141, 142] obtained using the parameters determined at the physical point. For the $m_\sigma = 500(400)$ MeV, the RQM model TCP at $(\mu_{\text{TCP}}, T_{\text{TCP}}) = (220.15, 71.52)((194.6, 65.9))$ MeV and CEP at $(\mu_{\text{CEP}}, T_{\text{CEP}}) = (265.42, 38.71)((243.12, 37.03))$ MeV, shift respectively to the TCP at $(\mu_{\text{TCP}}, T_{\text{TCP}}) = (194.3, 126.53)((164.21, 126.41))$ MeV and CEP at $(\mu_{\text{CEP}}, T_{\text{CEP}}) = (252.0, 94.6)((230.5, 93.8))$ MeV in the Log RPQM model whereas the shifted TCP lies at $(\mu_{\text{TCP}}, T_{\text{TCP}}) = (202.2, 108.14)((172.4, 107.28))$ MeV and the shifted CEP gets located at $(\mu_{\text{CEP}}, T_{\text{CEP}}) = (252.7, 70.9)((227.6, 73.6))$ MeV in the PolyLog-glue RPQM model.

The quark number susceptibility diverges at the CEP, hence it will be significantly enhanced in the vicinity of CEP. Therefore critical regions around the CEP are mapped by defining the contours of constant ratio of quark number susceptibilities which are normalized by the free quark gas susceptibility. The contours of the constant ratios $R_q = 2, 35$, are drawn for the QM, PolyLog-glue PQM, RQM, Log RPQM and PolyLog-glue RPQM model (with the $T_0 = T_c^{\text{glue}} = 187$ MeV for the Polyakov loop potential). The QM model (under no sea mean field approximation) critical regions for the $R_q = 2, 3$ contours are quite small and very much compressed in its temperature direction width while the Polyakov loop potential in the PolyLog-glue PQM model generates extremely pinched, compressed and very small critical regions. One gets large, smooth and somewhat symmetrical critical re-

gions in the RQM model for $m_\sigma = 400$ and 500 MeV due to the on-shell renormalization of parameters after consistently treating the quark one-loop vacuum corrections in the RQM model where the critical regions perpendicular to the crossover transition line are significantly broad. The Log RPQM model critical regions are significantly large with a larger spread on the μ axis and the contours have somewhat compressed width due to the absence of quark back reaction. The PolyLog-glue RPQM model critical regions, have larger spread on the T axis while their μ axis spread are relatively smaller in comparison to the case of Log RPQM model. One gets broader, somewhat round and smoother shape of critical regions where the compression in the width of the contours is quite small due to the effect of quark back reaction in the PolyLog-glue RPQM model. The sizes of the $R_q = 2, 35$ critical regions for the case of $m_\sigma = 500$ MeV, are noticeably larger than the corresponding critical regions obtained for the case of $m_\sigma = 400$ MeV in the RQM and RPQM (Log and PolyLog-glue) models because the CEP, of the different model settings for the $m_\sigma = 500$ MeV, lie at higher chemical potentials μ_{CEP} where the curvature (bending) of the phase boundary is larger. We have found that the TCP lies at the boundary of $R_q = 2$ critical region around the CEP when the $m_\sigma = 500$ MeV in the RQM model while the TCP lies noticeably away from the $R_q = 2$ critical region when the $m_\sigma = 400$ MeV, It means critical fluctuations around the CEP are likely to be influenced by the presence of TCP in RQM model when $m_\sigma = 500$ MeV. The Log RPQM and PolyLog-glue RPQM model TCP gets located quite well inside the critical region of the $R_q = 2$ contour around the CEP for the $m_\sigma = 500$ MeV while the TCP in these models for the case of $m_\sigma = 400$ MeV lies noticeably away from the the $R_q = 2$ contour. Therefore the critical fluctuations around the Log RPQM and PolyLog-glue RPQM model CEP when the $m_\sigma = 500$ MeV, will be affected by the presence of TCP nearby. The second aim of present work gets completely addressed in the above analysis.

In order to see how the different methods of treating quark one loop vacuum fluctuations, affect the phase diagram, its CEP location and critical fluctuations around it, the on-shell renormalized RQM, RPQM-I and RPQM-II model phase diagrams for the $m_\sigma = 400$ MeV, have been compared with the phase diagrams obtained in the curvature mass based parametrized work of Schaeffer et. al. in Ref. [118] for the QMVT, PQMVT-I and PQMVT-II model scenario. The PQMVT model is named as PQMVT-I when $T_0 = 270$ MeV for the pure gauge theory in the Log Polyakov loop potential while with the quark back reaction, the corresponding model scenario is termed as PQMVT-II model when the $T_0(\mu)$ is chemical potential dependent (where $T_0(\mu = 0) = 270$ MeV) in the Log Polyakov loop potential. The Log RPQM model setting is termed as RPQM-I model while the PolyLog-glue RPQM model scenario is renamed as RPQM-II model for the $m_\sigma = 400$

MeV case when we take $T_0 = 270$ MeV for the pure gauge Polyakov loop potential. The RQM model CEP is at $(\mu_{\text{CEP}}, T_{\text{CEP}}) = (243.12, 37.03)$ MeV while the QMVT model CEP lies at $(\mu_{\text{CEP}}, T_{\text{CEP}}) = (286.0, 32.0)$ MeV. The RPQM-I model CEP lies at $(\mu_{\text{CEP}}, T_{\text{CEP}}) = (237.8, 104.23)$ MeV whereas the PQMVT-I model CEP is at $(\mu_{\text{CEP}}, T_{\text{CEP}}) = (283.0, 90.0)$ MeV while in the presence of quark back reaction, the RPQM-II model CEP lies at the point $(\mu_{\text{CEP}}, T_{\text{CEP}}) = (228.54, 86.47)$ MeV and PQMVT-II model CEP gets located at the $(\mu_{\text{CEP}}, T_{\text{CEP}}) = (280.0, 83.0)$ MeV.

The RQM model critical regions are smooth, noticeably broad (perpendicular to the crossover transition line) and have similar spread as found for the QMVT model contours in the Ref. [118]. Having larger spread below the CEP on the T axis, the QMVT model contours get successively compressed developing a narrow neck like structure below the T_{CEP} because the CEP lies at higher chemical potential $\mu_{\text{CEP}} = 286$ MeV where the curvature of first order phase transition line is large. The above narrowing is almost non-existent for the RQM model contours below the T_{CEP} which are quite smooth because the CEP lies at significantly lower chemical potential $\mu_{\text{CEP}} = 243.12$ MeV where the first order transition line has noticeably smaller curvature. The total T axis spread of the PQMVT-I model critical region signified by the $R_q = 2$ susceptibility contour, is almost double the T axis size of the RPQM-I model critical region while the total spread of the PQMVT model critical region on the μ axis, is only about 10 MeV larger than the total μ axis size of the critical region found in the

RPQM-I model. The significantly large PQMVT-I model critical regions, become successively narrower below the T_{CEP} with a large compressed neck like structure as in the QMVT model. Here again the above feature is caused by the fact the CEP lies at a significantly higher chemical potential $\mu_{\text{CEP}} = 280$ MeV where the curvature of the first order transition line is quite large. In contrast to the above, the RPQM-I model CEP lies noticeably higher up and significantly left in the phase diagram at smaller chemical potential $\mu_{\text{CEP}} = 237.8$ MeV where the curvature of the first order transition line is small. Therefore one gets smooth, somewhat symmetrical critical regions in the RPQM-I model with a negligibly small compression in the width of contour below the CEP. The $R_q = 2$ critical region for the RPQM-II model has almost an equal spread on the T axis (53.1 MeV) and μ axis (54.2 MeV) due to effect of quark back reaction in the PolyLog-glue Polyakov loop potential. The RPQM-II model contours while being larger than the spread of RPQM-I model contours, are smoother, broader and do not have narrow neck like structure below its T_{CEP} . The PQMVT-II model critical regions with similar features as those of the PQMVT-I model, have smaller narrowing in the width of critical region below its T_{CEP} due to the effect of quark back reaction. The above analysis serves our third and last objective.

ACKNOWLEDGMENTS

Akanksha Tripathi acknowledges the support of CSIR Junior Research Fellowship. We are very much thankful to Pooja Kumari and Suraj Kumar Rai for valuable discussions and reading of the manuscript.

[1] N. Cabibbo and G. Parisi, *Phys.Lett.B* **59**, 67-69 (1975).
[2] L. D. McLerran and B. Svetitsky, *Phys. Rev. D* **24**, 450 (1981); B. Svetitsky, *Phys. Rep.* **132**, 1 (1986).
[3] B. Muller, *Rep. Prog. Phys.* **58**, 611 (1995).
[4] H. Meyer-Ortmanns, *Rev. Mod. Phys.* **68**, 473 (1996).
[5] D. H. Rischke, *Prog. Part. Nucl. Phys.* **52**, 197 (2004).
[6] A. Ali Khan et al. *Phys. Rev. D* **64**, 074510 (2001).
[7] S. Digal, E. Laermann and H. Satz, *Eur. Phys. J. C* **18**, 583 (2001).
[8] Z. Fodor, S. D. Katz, and K. K. Szabo, *Phys. Lett. B* **568**, 73 (2003).
[9] C. R. Allton, M. Doring, S. Ejiri, S. J. Hands, O. Kaczmarek, F. Karsch, E Laermann and K. Redlich, *Phys. Rev. D* **71**, 054508 (2005).
[10] F. Karsch, *J. Phys. G* **31**, S633 (2005).
[11] Y. Aoki, Z. Fodor, S. D. Katz and K. K. Szabo, *Phys. Lett. B* **643**, 46 (2006).
[12] M. Cheng et al., *Phys. Rev. D* **74**, 054507 (2006).
[13] M. Cheng et al., *Phys. Rev. D* **77**, 014511 (2008).
[14] J. Langelage, S. Lottini, and O. Philipsen, *J. High Energy Phys.* **02** (2011) 057.
[15] A. Bazavov et al., *Phys. Rev. D* **80**, 014504 (2009);
[16] S. Ejiri et al., *Phys. Rev. D* **80**, 094505 (2009).
[17] F. Karsch, *Lect. Notes Phys.* **583**, 209 (2002).
[18] M. G. Alford, A. Schmitt and K. Rajagopal, *Rev. Mod. Phys.* **80**, 1455 (2008).
[19] K. Fukushima and T. Hatsuda, *Rep. Prog. Phys.* **74**, 014001 (2011).
[20] G. Fejos, *Phys. Rev. D* **92**, 036011 (2015).
[21] G. Fejos, A. Hosaka, *Phys. Rev. D* **94**, 036005 (2016).
[22] Fabian Rennecke, Bernd-Jochen Schaefer, *Phys. Rev. D* **96**, 016009 (2017).
[23] G. Fejos, A. Hosaka, *Phys. Rev. D* **98**, 036009 (2018).
[24] G. Fejos, A. Patkos, *Phys. Rev. D* **105**, 096007 (2022).
[25] G. 't Hooft, *Phys. Rev. Lett.* **37**, 8 (1976);
[26] B. J. Schaefer and M. Wagner, *Phys. Rev. D* **79**, 014018 (2009).
[27] H. Meyer-Ortmanns and B. J. Schaefer, *Phys. Rev. D* **53**, 6586 (1996).
[28] J. T. Lenaghan, D. H. Rischke and J. Schaffner-Bielich, *Phys. Rev. D* **62**, 085008 (2000).
J. T. Lenaghan, D. H. Rischke, *J. Phys. G* **26**, 431 (2000).
[29] J. T. Lenaghan, *Phys. Rev. D* **63**, 037901 (2001).
[30] Pedro Costa, M. C. Ruivo, C. A. de Sousa and Yu. L. Kalinovsky, *AIP Conf. Proc.* **775**, 173-181 (2005).

[31] Pedro Costa, M. C. Ruivo, C. A. de Sousa and Yu. L. Kalinovsky, *Phys. Rev. D* **71**, 116002 (2005).

[32] K. Fukushima, *Phys. Rev. D* **77**, 114028 (2008); **78**, 039902(E) (2008).

[33] A. M. Polyakov, *Phys. Lett. B* **72**, 477 (1978).

[34] B. Svetitsky and L. G. Yaffe, *Nucl. Phys. B* **210**, 423 (1982).

[35] T. Banks and A. Ukawa, *Nucl. Phys. B* **225**, 145 (1983).

[36] R. D. Pisarski, *Phys. Rev. D* **62**, 111501(R) (2000).

[37] K. Fukushima, *Phys. Lett. B* **591**, 277 (2004).

[38] B. Layek, A. P. Mishra, A. M. Srivastava and V. K. Tiwari, *Phys. Rev. D* **73**, 103514 (2006).

[39] C. Ratti, M. A. Thaler, and W. Weise, *Phys. Rev. D* **73**, 014019 (2006).

[40] S. Roessner, C. Ratti and W. Weise, *Phys. Rev. D* **75**, 034007 (2007).

[41] B. J. Schaefer, J. M. Pawlowski, and J. Wambach, *Phys. Rev. D* **76**, 074023 (2007).

[42] B. J. Schaefer, M. Wagner, and J. Wambach, *Phys. Rev. D* **81**, 074013 (2010).

[43] B. J. Schaefer, M. Wagner and J. Wambach, CPOD(2009)017, arXiv:0909.0289

[44] H. Mao, J. Jin, and M. Huang, *J. Phys. G* **37**, 035001.

[45] U. S. Gupta and V. K. Tiwari, *Phys. Rev. D* **81**, 054019 (2010).

[46] L. M. Haas, R. Stiele, J. Braun, J. M. Pawlowski and J. Schaffner-Bielich, *Phys. Rev. D* **87**, 076004 (2013).

[47] P. M. Lo, B. Friman, O. Kaczmarek, K. Redlich, and C. Sasaki, *Phys. Rev. D* **88**, 074502 (2013).

[48] R. Stiele and J. Schaffner-Bielich, *Phys. Rev. D* **93**, 094014 (2016).

[49] T. K. Herbst, J. M. Pawlowski, and B.-J. Schaefer, *Phys. Lett. B* **696**, 58 (2011).

[50] T. K. Herbst, J. M. Pawlowski, and B.-J. Schaefer, *Phys. Rev. D* **88**, 014007 (2013).

[51] S. Borsányi, Z. Fodor, C. Hoelbling, S. D. Katz, S. Krieg, C. Ratti, and K. K. Szabó, *J. High Energy Phys.* **09** (2010) 73.

[52] S. Borsányi, G. Endrodi, Z. Fodor, A. Jakovac, S. D. Katz, S. Krieg, C. Ratti and K. K. Szabó, *JHEP* **11**, (2010) 077. ; S. Borsányi, Z. Fodor, C. Hoelbling, S. D. Katz, S. Krieg and K. K. Szabo, *Phys. Lett. B* **730** (2014) 99-104.

[53] A. Bazavov et al., *Phys. Rev. D* **85**, 054503 (2012); *Phys. Rev. D* **90**, 094503 (2014)

[54] R. D. Pisarski and F. Wilczek, *Phys. Rev. D* **29**, 338 (1984).

[55] M. Asakawa and K. Yazaki, *Nucl. Phys. A* **504**, 668, (1989).

[56] A. Barducci, R. Casalbuoni, S. De Curtis, R. Gatto, and G. Pettini, *Phys. Lett. B* **231**, 463 (1989); *Phys. Rev. D* **41**, 1610 (1990).

[57] J. Berges and K. Rajagopal, *Nucl. Phys. B* **538**, 215 (1999).

[58] Y. Hatta and T. Ikeda, *Phys. Rev. D* **67**, 014028 (2003).

[59] H. Fujii, *Phys. Rev. D* **67**, 094018 (2003).

[60] Fukushima, Kenji *Physics of Particles and Nuclei Letters.*

[61] P. Herrera-Siklody, J. I. Latorre, P. pascual and J. Taron, *Phys. Lett. B* **419**, 326 (1998).

[62] R. Escribano, F. S. Ling, M. H. G. Tytgat, *Phys. Rev. D* **62**, 056004 (2000)

[63] V. K. Tiwari, *Phys. Rev. D* **111**, 114014 (2025)

[64] V. K. Tiwari, *Phys. Rev. D* **112**, 054046 (2025)

[65] D. T. Son and M. A. Stephanov, *Phys. Rev. D* **70**, 056001 (2004); Y. Androdi, G. Fodor, S. D. Katz, and K. K. Szabo, *Nature (London)* **443**, 675 (2006); S. Gupta, X. Luo, B. Mohanty, H. G. Ritter, and N. Xu, *Science* **332**, 1525 (2011).

[66] M. A. Stephanov, K. Rajagopal, and E. V. Shuryak, *Phys. Rev. D* **60**, 114028 (1999); *Phys. Rev. Lett.* **81**, 4816 (1998).

[67] B. Berdnikov and K. Rajagopal, *Phys. Rev. D* **61**, 105017 (2000).

[68] S. Jeon and V. Koch, *Phys. Rev. Lett.* **85**, 2076 (2000).

[69] S. Ejiri, F. Karsch, and K. Redlich, *Phys. Lett. B* **633**, 275 (2006).

[70] J. Adams et al. (STAR Collaboration), *Nucl. Phys. A* **757**, 102 (2005); M. Aggarwal et al. (STAR Collaboration), *Phys. Rev. Lett.* **105**, 022302 (2010).

[71] G. Odyniec; RHIC Beam Energy Scan Program: Phase I and II, *PoS CPOD 2013*, 043(2013) and *PoS CORFU2018* 151 (2019).

[72] C. Liu et al. 13th Int. Particle Acc. Conf. WEPOPT032

[73] Pandav, Ashish; *EPJ Web Conf.* **296**, 01016, (2024) ; A. Pandav (STAR collaboration), plenary talk at CPOD 2024, .

[74] M. Stephanov, *EPJ Web of Conferences* **314**, 00042 (2024)

[75] A. Bzdak, S. Esumi, V. Koch, J. Liao, M. Stephanov, N. Xu, *Phys. Rept.* **853**, 1 (2020).

[76] L. Du, A. Sorensen, M. Stephanov *Int. J. Mod. Phys. E* **33** (2024) **07**, 2430008.

[77] M.A. Stephanov, *Phys. Rev. Lett.* **102**, 032301 (2009).

[78] C. Athanasiou, K. Rajagopal, and M. Stephanov, *Phys. Rev. D* **82**, 074008 (2010).

[79] B. Mohanty, *Nucl. Phys. A* **830**, 899c (2009); X. Luo, B. Mohanty, H. G. Ritter, and N. Xu, *Phys. At. Nucl.* **75**, 676 (2012).

[80] M. A. Stephanov, *Phys. Rev. Lett.* **107**, 052301 (2011).

[81] Xin An, Marcus Bluhm, Lipei Du and Gerald V. Dunne et. All *Nuclear Physics A*,1017,(2022).

[82] Akamatsu Yukinao and Teaney Derek and Yan Fanglida and Yin Yi *Phys. Rev. C* **100**, 044901 (2019).

[83] V. Vovchenko, V. Koch and C. Shen, *Phys. Rev. C* **105**, 014904 (2022).

[84] X. An, G. Basar, M. Stephanov, H.U. Yee, *Phys. Rev. Lett.* **127**, 072301 (2021). *Phys. Rev. C* **108**, 034910 (2023).

[85] M. Pradeep, K. Rajagopal, M. Stephanov, Y. Yin, Freezing out fluctuations in Hydro+ near the QCD critical point, *Phys. Rev. D* **106**, 036017 (2022); M.S. Pradeep, M. Stephanov, *Phys. Rev. Lett.* **130**, 162301 (2023).

[86] P. Parotto, M. Bluhm, D. Mrocze, M. Nahrgang, J. Noronha-Hostler, K. Rajagopal, C. Ratti, T. Schäfer, M. Stephanov, *Phys. Rev. C* **101**, 034901 (2020).

[87] J.M. Karthein, M.S. Pradeep, K. Rajagopal, M. Stephanov, Y. Yin, Equilibrium expectations for non-Gaussian fluctuations near a QCD critical point, in 21st 8 838-839 International Conference on Strangeness in Quark Matter 2024 *arXiv:2409.16249 (nucl-th)*

[88] D. Roder, J. Ruppert and D. H. Rischke, *Phys. Rev. D* **68**, 016003 (2003).

[89] K. Fukushima, K. Kamikado and B. Klein, *Phys. Rev. D* **83**, 116005 (2011).

[90] M. Grahl and D. H. Rischke, *Phys. Rev. D* **88**, 056014 (2013).

[91] A. Jakovac, A. Patkos, Z. Szep, and P. Szepfalusy, *Phys. Lett. B* **582**, 179 (2004).

[92] T. Herpay, A. Patkós, Zs. Szép and P. Szépfalusy, *Phys. Rev. D* **71**, 125017 (2005).

[93] T. Herpay and Zs. Szép, *Phys. Rev. D* **74**, 025008 (2006).

[94] P. Kovács and Zs. Szép, *Phys. Rev. D* **75**, 025015 (2007).

[95] P. Kovacs and Zs. Szep, *Phys. Rev. D* **75**, 025015 (2007).

[96] T. Kahara and K. Tuominen, *Phys. Rev. D* **78**, 034015 (2008); **80**, 114022 (2009); **82**, 114026 (2010).

[97] E. S. Bowman and J. I. Kapusta, *Phys. Rev. C* **79**, 015202 (2009); J. I. Kapusta, and E. S. Bowman, *Nucl. Phys. A* **830**, 721C (2009).

[98] G. Fejos, A. Patkos, *Phys. Rev. D* **82**, 045011 (2010).

[99] A. Jakovac and Zs. Szep, *Phys. Rev. D* **82**, 125038, (2010).

[100] L. Ferroni, V. Koch, and M. B. Pinto, *Phys. Rev. C* **82**, 055205 (2010).

[101] G. Marko and Zs. Szep, *Phys. Rev. D* **82**, 065021 (2010).

[102] Gergely Fejős and András Patkós, *Phys. Rev. D* **112**; 7, 076013 (2025).

[103] O. Scavenius, A. Mocsy, I. N. Mishustin, and D. H. Rischke, *Phys. Rev. C* **64**, 045202 (2001).

[104] A. Mocsy, I. N. Mishustin, and P. J. Ellis, *Phys. Rev. C* **70**, 015204 (2004).

[105] B.-J. Schaefer and J. Wambach, *Nucl. Phys. A* **757**, 479 (2005).

[106] B.-J. Schaefer and J. Wambach, *Phys. Rev. D* **75**, 085015 (2007).

[107] A. Halasz, A. D. Jackson, R. E. Shrock, M. A. Stephanov, and J. J. M. Verbaarschot, *Phys. Rev. D* **58**, 096007 (1998).

[108] V. Skokov, B. Friman, E. Nakano, K. Redlich, and B.-J. Schaefer, *Phys. Rev. D* **82**, 034029 (2010).

[109] L. F. Palhares and E. S. Fraga, *Phys. Rev. D* **78**, 025013 (2008).

[110] E. S. Fraga, L. F. Palhares, and M. B. Pinto, *Phys. Rev. D* **79**, 065026 (2009).

[111] L. F. Palhares and E. S. Fraga, *Phys. Rev. D* **82**, 125018 (2010).

[112] R. Gatto, M. Ruggieri, *Phys. Rev. D* **82**, 054027 (2010).

[113] A. J. Mizher, M. N. Chernodub, and E. S. Fraga, *Phys. Rev. D* **82**, 105016 (2010).

[114] R. Khan and L. T. Kyllingstad, *AIP Conf. Proc.* **1343**, 504 (2011).

[115] U. S. Gupta, V. K. Tiwari, *Phys. Rev. D* **85**, 014010 (2012).

[116] S. Chatterjee and K. A. Mohan, *Phys. Rev. D* **85**, 074018 (2012).

[117] V. K. Tiwari, *Phys. Rev. D* **86**, 094032 (2012).

[118] B.-J. Schaefer and M. Wagner, *Phys. Rev. D* **85**, 034027 (2012).

[119] J. O. Andersen and A. Tranberg, *J. High Energy Phys.* **08** (2012) 002.

[120] D. Kharzeev, K. Landsteiner, A. Schmitt, H.-U. Yee (Eds.), *Strongly Interacting Matter in Magnetic Fields*, Lecture Notes in Phys. 871, Springer (2013).

[121] V. K. Tiwari, *Phys. Rev. D* **88**, 074017 (2013).

[122] J. Weyrich, N. Strodtthoff, and L. von Smekal, *Phys. Rev. C* **92**, 015214 (2015).

[123] M. Drew, W. Weise, *Phys. Rev. C* **91**, 035802 (2015).

[124] P. Kovács, Zs. Szép, Gy. Wolf, *Phys. Rev. D* **93**, 114014 (2016).

[125] Andreas Zacchi and Jürgen Schaffner-Bielich, *Phys. Rev. D* **97**, 074011 (2018).

[126] Andreas Zacchi and Jürgen Schaffner-Bielich, *Phys. Rev. D* **100**, 0123024 (2019).

[127] S. K. Rai and V. K. Tiwari, *Eur. Phys. J. Plus* **135**:844, (2020).

[128] L. Brandes, N. Kaiser, W. Weise, *Eur. Phys. J. A* **57**:243, (2021).

[129] R. Kobes, G. Kunstatter, and A. Rebhan, *Phys. Rev. Lett.* **64**, 2992 (1990); *Nucl. Phys. B* **355**, 1 (1991).

[130] A. K. Rebhan, *Phys. Rev. D* **48**, R3967 (1993).

[131] K. Kajantie, M. Laine, K. Rummukainen, and M. E. Shaposhnikov *Nucl. Phys. B* **458**, 90 (1996).

[132] S. Carignano, M. Buballa and B-J Schaefer *Phys. Rev. D* **90**, 014033 (2014).

[133] S. Carignano, M. Buballa, and W. Elkamhawy, *Phys. Rev. D* **94**, 034023 (2016).

[134] J. O. Andersen, W. R. Naylor, and A. Tranberg, *Rev. Mod. Phys.* **88**, 025001 (2016).

[135] P. Adhikari, J. O. Andersen and P. Kneschke, *Phys. Rev. D* **95**, 036017 (2017).

[136] P. Adhikari, J. O. Andersen and P. Kneschke, *Phys. Rev. D* **96**, 016013 (2017).

[137] P. Adhikari, J. O. Andersen and P. Kneschke, *Phys. Rev. D* **98**, 074016 (2018).

[138] A. Folkestad, J. O. Andersen, *Phys. Rev. D* **99**, 054006 (2019).

[139] S. K. Rai and V. K. Tiwari, *Phys. Rev. D* **105**, 094010 (2022).

[140] S. K. Rai and V. K. Tiwari, *Phys. Rev. D* **108**, 074014 (2023).

[141] V. K. Tiwari, *Phys. Rev. D* **108**, 074002 (2023).

[142] S. K. Rai and V. K. Tiwari, *Phys. Rev. D* **109**, 034025 (2024).

[143] Jens O. Andersen and Mathias P. Nødtvedt, arXiv:2506.02941.

[144] Hosein Gholami, Kurth Lennart, Ugo Mire, Michael Buballa, and Bernd-Jochen Schaefer, arXiv:2505.22542.

[145] D. A. Clarke, P. Dimopoulos, F. Di Renzo, J. Goswami, C. Schmidt, S. Singh, K. Zambello arXiv:2405.10196 [hep-lat]

[146] G. Basar, *Phys. Rev. C* **110**, 015203, (2024)

[147] M. Hippert, J. Grefa, T. A. Manning, J. Noronha, J. Noronha-Hostler, I. P. Vazquez, C. Ratti, R. Rougemont, M. Trujillo, *Phys. Rev. D* **110**, 094006 (2024).

[148] Y. Lu, F. Gao, Y.X. Liu, J.M. Pawłowski, *Phys. Rev. D* **110**, 014036 (2024)

[149] Juan Xiong, Meng Jin, and Jiarong Li *Phys. Rev. C* **83**, 025204 (2011)